

THE EFFECTS OF BINARY STARS ON INFERRRED  
REMNANT POPULATIONS IN GLOBULAR CLUSTERS

by

Peter Smith

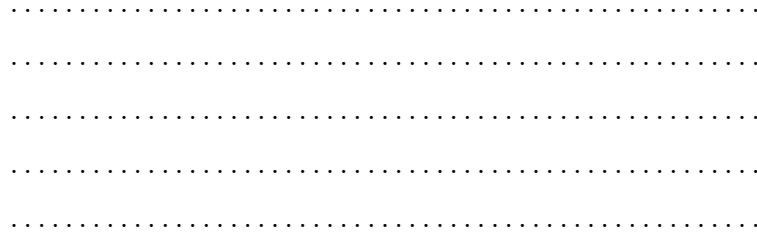
A THESIS SUBMITTED IN PARTIAL FULFILMENT OF  
THE REQUIREMENTS FOR THE DEGREE OF

BACHELOR OF SCIENCE

in

Honours Astrophysics

(Department of Astronomy and Physics, Dr. Vincent Hénault-Brunet supervising  
faculty)



SAINT MARY'S UNIVERSITY

May 11, 2022

© Peter Smith, 2022

## ABSTRACT

### THE EFFECTS OF BINARY STARS ON INFERRED REMNANT POPULATIONS IN GLOBULAR CLUSTERS

by *Peter Smith*

submitted on May 11, 2022:

Current, state-of-the-art equilibrium mass models of globular clusters assume that all stars are single, making the effects of binary systems an unknown quantity. In this thesis we develop a method to include realistic binary populations in these models. We use our method to fit three sets of models with varying binary fractions to observations of the globular cluster 47 Tuc. All three sets of models are able to reproduce all observables and differ almost exclusively in their recovered mass function slopes and black hole content while retaining consistent estimates for structural parameters. Models with binary fractions of 0%, 2% and 10% have inferred black hole populations with masses of  $135_{-92}^{+104} M_{\odot}$ ,  $114_{-79}^{+144} M_{\odot}$  and  $81_{-81}^{+121} M_{\odot}$  respectively, showing that the inferred black hole content decreases when increasing the assumed binary fraction. We show that this effect is due to binary stars filling a similar role to black holes in the central mass distribution of the cluster indicating that there exists a degeneracy between the adopted binary fraction and the inferred black hole content for some clusters. We further discuss the implications of these results for past and future works.

# Contents

<b>Contents</b> . . . . .	iii
<b>List of Figures</b> . . . . .	v
<b>List of Tables</b> . . . . .	xii
<b>1 Introduction</b> . . . . .	1
1.1 Globular Clusters . . . . .	1
1.2 Modelling Globular Clusters . . . . .	5
1.3 Binary Stars . . . . .	9
1.3.1 Binaries in Globular Clusters . . . . .	9
1.3.2 Observations of Binary Stars in Globular Clusters . . . . .	12
1.4 This Thesis . . . . .	16
<b>2 Methods</b> . . . . .	18
2.1 Data . . . . .	18
2.1.1 Kinematics and density profiles . . . . .	18
2.1.2 Stellar mass functions . . . . .	19
2.1.3 Pulsar Data . . . . .	20
2.2 Binary Fraction Measurements . . . . .	20

2.3	Generating mass functions . . . . .	21
2.3.1	Single Star Mass Functions . . . . .	21
2.3.2	Binary Mass Functions . . . . .	22
2.4	Fitting Models to Data . . . . .	27
2.4.1	Likelihoods . . . . .	27
2.4.2	Fitting Mass Functions to Observations . . . . .	33
<b>3</b>	<b>Results</b> . . . . .	36
3.1	Previous Results . . . . .	36
3.2	Low Binary Fraction . . . . .	38
3.3	High Binary Fraction . . . . .	42
<b>4</b>	<b>Discussion</b> . . . . .	44
4.1	The Effects of the Binaries . . . . .	44
<b>5</b>	<b>Conclusion</b> . . . . .	49
5.1	Future Work . . . . .	50
<b>A</b>	<b>Supplementary Material</b> . . . . .	52
	<b>Bibliography</b> . . . . .	68

# List of Figures

1.1	The globular cluster NGC 7006 imaged by the Hubble Space Telescope's Advanced Camera for Surveys, photo courtesy of ESA/Hubble & NASA . . . . .	2
1.2	Mean mass of objects within a realistic model of the globular cluster 47 Tuc, as a function of distance from the cluster centre. The concentration of high-mass objects in the central regions of the cluster is obvious, as is the preference for low-mass objects in the outskirts of the cluster, clearly demonstrating the effects of mass segregation. . . . .	4
1.3	A simple LIMEPY model with four components with differing <i>mean</i> masses but equal <i>total</i> masses. The lighter components have higher velocity dispersions and are less centrally concentrated while the more massive components have lower velocity dispersions and are more centrally concentrated. . . . .	7
1.4	The line-of-sight velocity dispersion profile and number density profile of bright stars in 47 Tuc, simultaneously fit by a LIMEPY model. The LIMEPY models are able to very accurately reproduce a range of cluster observables including simultaneous fitting of stellar mass function data and kinematic data. . . . .	8



2.1 The evolution of a typical mass function from $t = 0$ to $t = 10$ Gyr. The stellar bins are plotted in green while the remnant bins are plotted in black, the current main-sequence turn-off is plotted as a dashed black line. As the cluster ages, more and more main sequence stars evolve into remnants. The lack of mass loss in the low-mass regime is evident, we set the mass loss due to escaping stars to be zero, meaning that we are effectively fitting on the present-day mass function for low-mass stars. Lower right: The evolution of the total mass of the cluster is plotted as a fraction of the initial mass. Mass loss is dominated by the effects of stellar evolution but also has contributions from ejected heavy remnants. . . . .	23
2.2 The resulting mass ratio distributions for the “flat” and “solar” mass ratio distributions. Both distributions are truncated and lowered at $q = 0.2$ due to the relative lack of low very low mass stars within the mass functions, making the creation of binary systems with a very low mass ratio impossible. . . . .	24

2.3 The main-sequence portion of a mass function before and after binaries are added. $M_j$ is the total mass within a bin while $m_j$ is the mean mass of the bin. The blue circles are the original main sequence bins and the crosses are the modified main sequence bins. The orange crosses show the single stars after mass has been removed to create binaries and the many green crosses are the binary bins that are initially created. The red crosses are the rebinned binary bins which are actually used in the computation of the LIMEPY models. . . . .	26
2.4 The resulting probability distribution for the spin period derivative of pulsar 47Tuc S from the method described above for the best-fitting models of 47Tuc. The green line is the likelihood of a given period derivative measurement given the best-fitting model parameters and the yellow line is the measured spin period derivative. The asymmetry in the distribution is due to the intrinsic spin-down of the pulsar, biasing the distribution to positive values of $\dot{P}/P$ . . . . .	32
2.5 Relation between stellar mass and luminosity through HST/WFC3's F814W filter, derived from a MIST isochrone. The F814W filter is used to replicate the original observations, see Sollima & Baumgardt (2017) for further details. . . . .	35
3.1 Distribution in mass and number of black holes for models with a 0% binary fraction. . . . .	37
3.2 Model fits to observables for models with a 2% binary fraction. . . . .	39

3.3	Model fits to stellar mass function data for models with a 2% binary fraction. . . . .	40
3.4	Distribution in mass and number of black holes for models with a 2% binary fraction. . . . .	41
3.5	Distribution of mass in binaries for models with a 2% binary fraction. . . . .	41
3.6	Distribution in mass and number for models with a 10% binary fraction. . . . .	43
3.7	Distribution of mass in binaries for models with a 10% binary fraction. . . . .	43
4.1	Enclosed mass profiles for the stellar remnants in the $f_b = 0\%$ model and the remnants and remnants plus binaries in the $f_b = 10\%$ model. The two remnant profiles are very different between the $f_b = 0\%$ and $f_b = 10\%$ cases which mirrors the lower black hole content. The most interesting part of these profiles is the fact that when the <i>binaries</i> are added to the remnants the enclosed mass profiles match very well. This demonstrates very clearly that the binaries are filling the same role as the heavy remnants in the central regions of the cluster and explains why adding binaries reduces the need for black holes in the models. . . . .	46
4.2	Posterior probability distributions of mass and number of BHs in each set of models. Distributions are represented by a Gaussian kernel density estimator of the discrete values for easier visual comparison. . . . .	47
4.3	Mass density profiles for the models with a binary fraction of 10% . . . . .	48

A.1 Maximum acceleration profiles for set of best-fit models with a 0% binary fraction. The accelerations of the pulsars, as derived from their period derivates, are plotted with accelerations derived from orbital periods in blue and upper limits for accelerations derived from spin periods in orange. All accelerations are consistent with the maximum acceleration allowed by the model within their $1\sigma$ credibility intervals.	55
A.2 Probability distributions for measurements of orbital period derivatives for a set of best-fit models with a 0% binary fraction. The measured period derivates for each pulsar are plotted in orange. . . . .	56
A.3 Probability distributions for measurements of spin period derivatives for a set of best-fit models with a 0% binary fraction. The measured period derivates for each pulsar are plotted in orange. . . . .	57
A.4 Trace plot showing the evolution of the MCMC chain for model with a 0% binary fraction. . . . .	58
A.5 Corner plot showing the marginalized posterior probability distributions of models parameters with a 0% binary fraction. . . . .	59
A.6 Trace plot showing the evolution of the MCMC chain for model with a 2% binary fraction. . . . .	60
A.7 Corner plot showing the marginalized posterior probability distributions of models parameters with a 2% binary fraction. . . . .	61
A.8 Trace plot showing the evolution of the MCMC chain for model with a 10% binary fraction. . . . .	62

A.9 Corner plot showing the marginalized posterior probability distributions of models parameters with a 10% binary fraction. . . . .	63
A.10 Model fits to the observables for models with no binary stars. . . . .	64
A.11 Model fits to stellar mass function data for models with no binary stars.	65
A.12 Model fits to the observables for models with a 10% binary fraction. .	66
A.13 Model fits to the stellar mass function data for models with a 10% binary fraction. . . . .	67

# List of Tables

2.1	Model parameters and their priors. Most priors are uniform and are chosen to bound the chains around a reasonable range of parameter values for 47 Tuc. For the mass function slopes we add the additional constraint that $\alpha_2$ must be steeper than $\alpha_1$ and $\alpha_3$ steeper than $\alpha_2$ to ensure that we are only testing mass functions that make sense physically. For the distance we use a Gaussian prior with the distance measurement from Baumgardt & Vasiliev (2021) providing the mean and standard deviation of the prior. . . . .	28
3.1	Best-fit parameters with $1\sigma$ credibility intervals for models with a binary fraction of 0% . . . . .	37
3.2	Best-fit parameters with $1\sigma$ credibility intervals for models with a 2% binary fraction. . . . .	38
3.3	Best-fit parameters with $1\sigma$ credibility intervals for models with a 10% binary fraction. . . . .	42
4.1	Best-fit parameters with $1\sigma$ credibility intervals for all sets of models.	45
4.2	Black hole content in each set of models . . . . .	47

A.1 Pulsar timing data for 47 Tuc, spin periods. Reference key is as follows:  
 a:Freire & Ridolfi (2018), b:Freire et al. (2017), c:Ridolfi et al. (2016) 53

A.2 Pulsar timing data for 47 Tuc, orbital periods. Reference key is as follows: a:Freire & Ridolfi (2018), b:Freire et al. (2017), c:Ridolfi et al. (2016) 54

# Chapter 1

## Introduction

### 1.1 Globular Clusters

Globular clusters (GCs) are dense, spheroidal collections of hundreds of thousands of stars with total masses ranging from  $10^4$  to  $10^6$  solar masses that are bound by their own self-gravity. GCs are found in most galaxies, with the Milky Way hosting roughly 150, mostly located in the outer halo (e.g. Heggie & Hut, 2003). GCs represent some of the oldest stellar populations in the universe and are usually in excess of 10 billion years old. Figure 1.1 shows the globular cluster NGC 7006, imaged by the Hubble Space Telescope's Advanced Camera for Surveys. The dense core of the cluster is clearly visible and is made up of tens of thousands of stars. The dynamics of globular clusters are almost entirely governed by the interactions between individual cluster members, with small effects from the galactic potential of its host galaxy as well as mass loss due to stellar evolution. Two-body relaxation is the main driver of the evolution of GCs and, through this process, they display a wide range of dynamical phenomena. Among these phenomena, mass segregation is a process through which heavier objects migrate to the centre of a cluster and lighter objects move to the outer regions. As objects interact with each other, their kinetic energies will tend to equalize which leads to heavier objects slowing down and lighter objects speeding up



Figure 1.1: The globular cluster NGC 7006 imaged by the Hubble Space Telescope’s Advanced Camera for Surveys, photo courtesy of ESA/Hubble & NASA

(e.g. Heggie & Hut, 2003). This process leads to the core of the cluster containing a much higher proportion of high-mass stars and heavy remnants than the rest of the cluster. Figure 1.2 shows the mean mass of objects within a realistic model of a globular cluster as a function of distance from the cluster centre. The regions closest to the core of the cluster have a much higher mean mass due to the increased presence of heavy remnants and high-mass stars caused by the effects of mass segregation.

The study of stellar remnants in globular clusters has far-reaching implications for diverse fields of astrophysics. Due to the effects of mass segregation and the high

densities within the cores of globular clusters, the central regions of globular clusters are an ideal environment for mergers of compact objects, especially in the early stages of their evolution when they are significantly denser than at the present day (e.g. Portegies Zwart et al., 2004; Rodriguez et al., 2022). These mergers can be detected through their resultant gravitational waves and the expected rates for gravitational wave events (in particular black hole-black hole mergers) depend significantly on the compact object populations in globular clusters (e.g Weatherford et al., 2021). These mergers are also thought to be one of the most promising formation channels for intermediate-mass black holes (IMBHs) (e.g. Giersz et al., 2015), a so-far undetected class of black holes whose masses fall between those of stellar-mass black holes and those of supermassive black holes. This means that globular clusters are one of the most commonly proposed candidates to host intermediate-mass black holes. The formation of these black holes has important implications for understanding the formation of the supermassive black holes that we find at the centre of galaxies.

The work presented in this thesis builds on a previous project I worked on which used pulsar timing data to constrain the properties of the globular cluster 47 Tuc. In that work, we were able to place stringent limits on the mass in dark remnants (black holes, neutron stars, white dwarfs) within the cluster, establishing strong constraints on the black hole content specifically. While this project was able to fully account for effects like mass segregation and uncertain mass functions, one limitation of the models that it used (which we will discuss in the following section) was the assumption that all objects within the cluster are single. Because the masses of some binary stars are higher than the typical masses of objects within the cluster, they too will mass

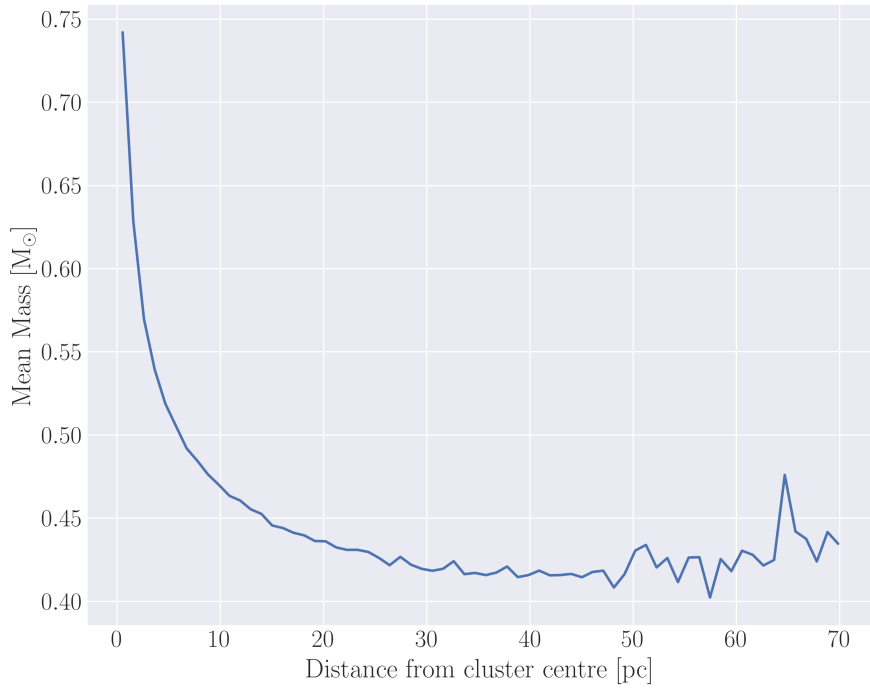


Figure 1.2: Mean mass of objects within a realistic model of the globular cluster 47 Tuc, as a function of distance from the cluster centre. The concentration of high-mass objects in the central regions of the cluster is obvious, as is the preference for low-mass objects in the outskirts of the cluster, clearly demonstrating the effects of mass segregation.

segregate to the core of the cluster like heavy stellar remnants. While the binary fraction in 47 Tuc is expected to be low (Milone et al., 2012), the effects that a centrally concentrated population of binary stars might have on the inferred remnant content of the cluster is still unclear and worth investigating. In particular, there may be a degeneracy between the assumed binary fraction and the inferred black hole content of a cluster. The dynamical effects of a small population of black holes and a small population of centrally concentrated binaries could be very similar which makes the inclusion of binaries important for models attempting to constrain the black hole content of a cluster.

## 1.2 Modelling Globular Clusters

When modelling the dynamics of globular clusters, there are generally two approaches commonly used. The first is to model the entire evolutionary history of the cluster from initial conditions to the present day. The most commonly employed versions of these “evolutionary models” are direct  $N$ -body integration (see for example Baumgardt 2017), which directly calculate the gravitational interactions between each object in the cluster, and Monte Carlo models (e.g. Rodriguez et al. 2022, Hypki & Giersz 2013), which approximate the gravitational interactions between objects according to the method of Hénon (1971). While these models provide insight into the dynamical history of the cluster, they are very computationally expensive with even the fastest models taking on the order of a day to model a realistic globular cluster (Rodriguez et al., 2022).

The second approach is to model just the present-day conditions of the cluster. These models, which we call “equilibrium models”, capture none of the dynamical history of the cluster but fully describe the present-day state of the cluster. These equilibrium models are much less computationally demanding than evolutionary models. Their relative efficiency allows us to explore a significantly larger parameter space when fitting the models to observations to constrain the present-day properties of a cluster. In particular, it is worth highlighting that by using equilibrium models, we are able to vary the stellar mass function of the cluster as well as the black hole and remnant retention fractions with more flexibility than what might be possible with evolutionary models, due to the computational cost of computing extensive grids

---

of evolutionary models with many parameters varied in the initial conditions (e.g. various stellar initial mass functions, initial cluster radii, masses, etc.).

The comparative efficiency of these models further enables the use of statistical fitting techniques like Markov chain Monte Carlo (MCMC) or Nested Sampling which would be prohibitively expensive to use with evolutionary models. This means that instead of computing a grid of models and finding the “best-fitting” model we can instead recover posterior probability distributions for key cluster parameters.

In this work, we use the LIMEPY family of models presented by Gieles & Zocchi (2015). The LIMEPY models are a set of distribution function-based equilibrium models that are isothermal for the most bound stars near the cluster centre and described by polytropes in the outer regions near the escape energy. The models have been extensively tested against  $N$ -body models (Zocchi et al., 2016; Peuten et al., 2017) and are able to effectively reproduce the effects of mass segregation. Their suitability for mass modelling globular clusters has been tested on mock data (Hénault-Brunet et al., 2019) and they have recently been applied to real datasets as well (e.g. Gieles et al., 2018; Hénault-Brunet et al., 2020).

Figure 1.3 shows the density and velocity dispersion profiles for a simple LIMEPY model with four components. The lightest components have the highest velocity dispersion and the most massive components are the most centrally concentrated.

The input parameters needed to compute our models include the central concentration parameter  $W_0$ , the truncation parameter  $g^1$ , the anisotropy radius  $r_a$  which

---

<sup>1</sup>Several well-known classes of models are reproduced by specific values of  $g$ : Woolley models (Woolley, 1954) have  $g = 0$ , King models (King, 1966)  $g = 1$ , and Wilson models (Wilson, 1975)  $g = 2$ .

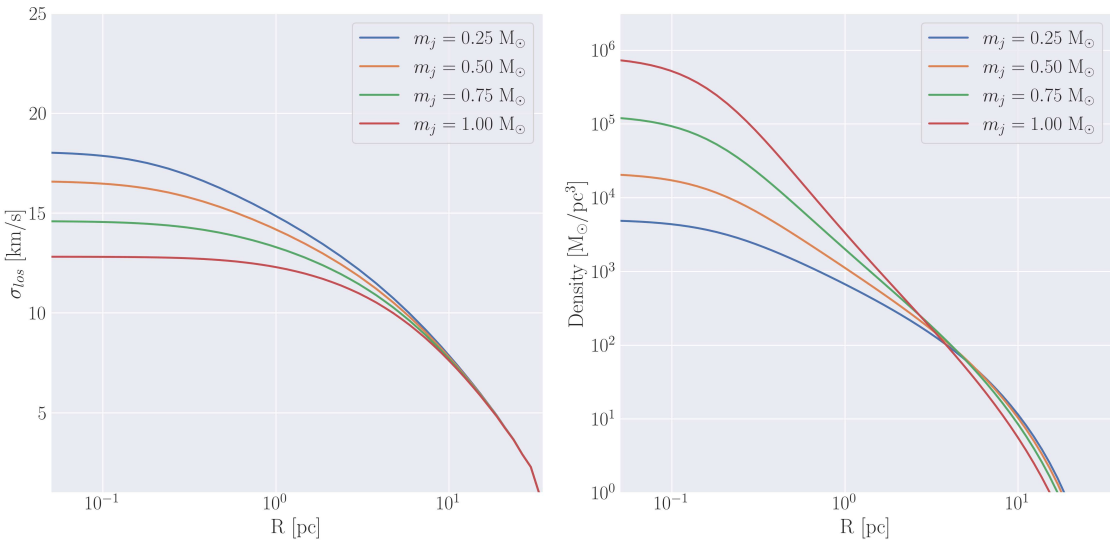


Figure 1.3: A simple LIMEPY model with four components with differing *mean* masses but equal *total* masses. The lighter components have higher velocity dispersions and are less centrally concentrated while the more massive components have lower velocity dispersions and are more centrally concentrated.

determines the degree of radial anisotropy in the models,  $\delta$  which sets the mass dependence of the velocity scale and thus governs the degree of mass segregation, and finally the specific mass bins to use as defined by the mean stellar mass ( $m_j$ ) and total mass ( $M_j$ ) of each bin, which together specify the stellar mass function. In order to scale the model units into physical units, the total mass of the cluster  $M$  and a size scale (the half-mass radius of the cluster  $r_h$ ) are provided as well. Finally, we provide the distance to the cluster ( $d$ ) which is used in converting between angular and linear quantities. Figure 1.4 demonstrates the ability of the models to simultaneously fit many cluster observables, specifically pictured are the line-of-sight velocity dispersion profile and the number density profile of bright stars. The power of these models lies in their ability to simultaneously fit not just kinematic and number density data but also the stellar mass function data of a cluster, Figure 1.5 shows model fits to stellar

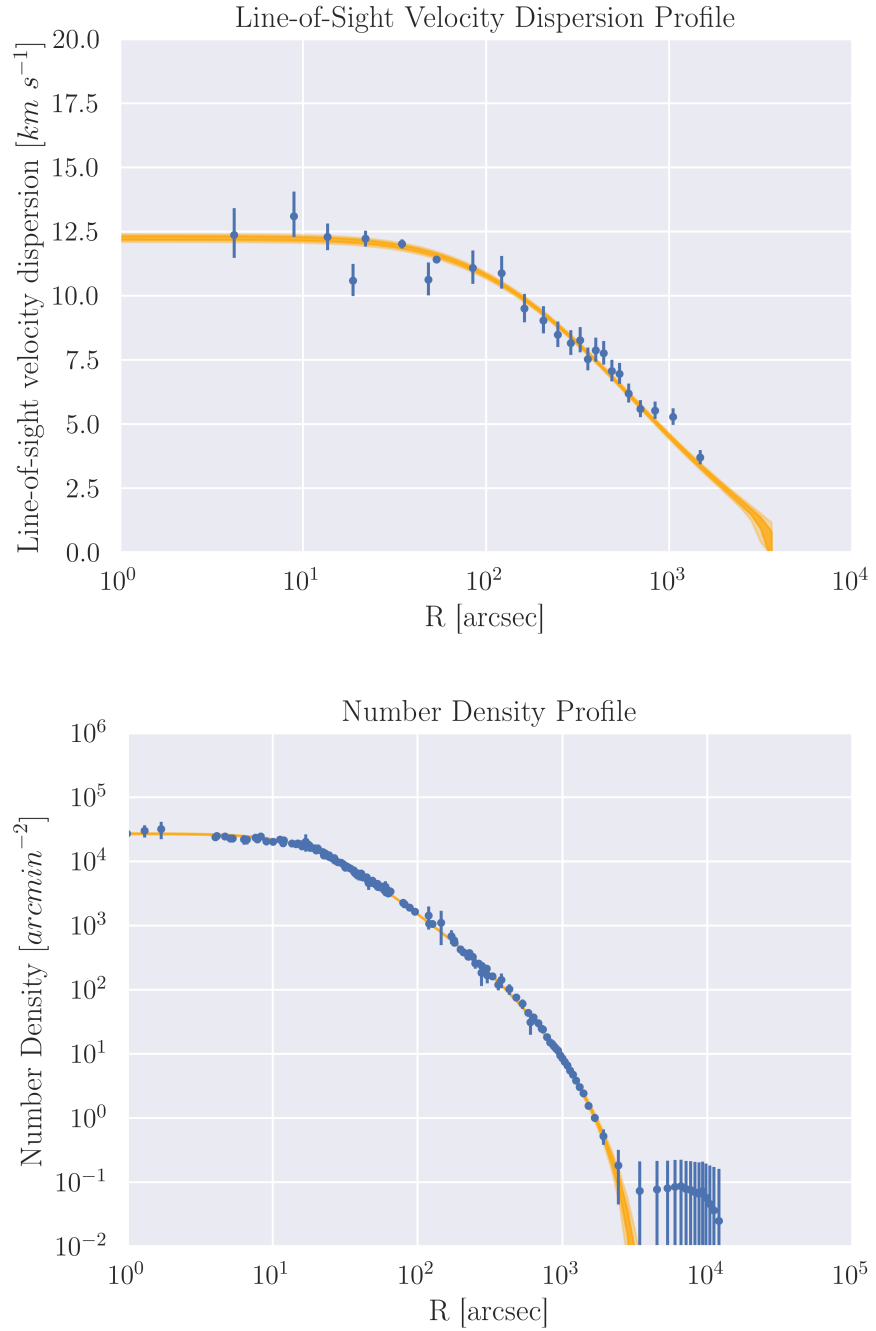


Figure 1.4: The line-of-sight velocity dispersion profile and number density profile of bright stars in 47 Tuc, simultaneously fit by a LIMEPY model. The LIMEPY models are able to very accurately reproduce a range of cluster observables including simultaneous fitting of stellar mass function data and kinematic data.

mass function data from the globular cluster 47 Tuc.

In their current implementation, these models assume that all objects within the cluster are single and make no attempt to model the dynamical effects of stellar multiplicity. In this thesis, we adapt these models to incorporate some of the effects of binary stars under the assumption that binaries with very long periods have been ionized by the present day. This allows us to treat binary systems as point masses and lets us model their dynamics by simply moving some of the mass in stars into heavier bins according to the specified binary population.

## 1.3 Binary Stars

### 1.3.1 Binaries in Globular Clusters

In general, the binary systems found within present-day clusters differ significantly from the field binaries that are more easily observed. In particular, we expect very few long-period binaries, on account of them being ionized by the frequent interactions with other cluster members (Heggie & Hut, 2003). We frequently use the terms “hard” and “soft” to describe binaries, where “soft binaries” have binding energies less than or comparable to the average kinetic energy of a cluster member while “hard binaries” have larger binding energies. Due to the frequent interactions within clusters, we expect that all soft binaries have long since been ionized by the present day leaving only a population of hard binaries with a truncated period distribution compared to field binaries (Heggie & Hut, 2003).

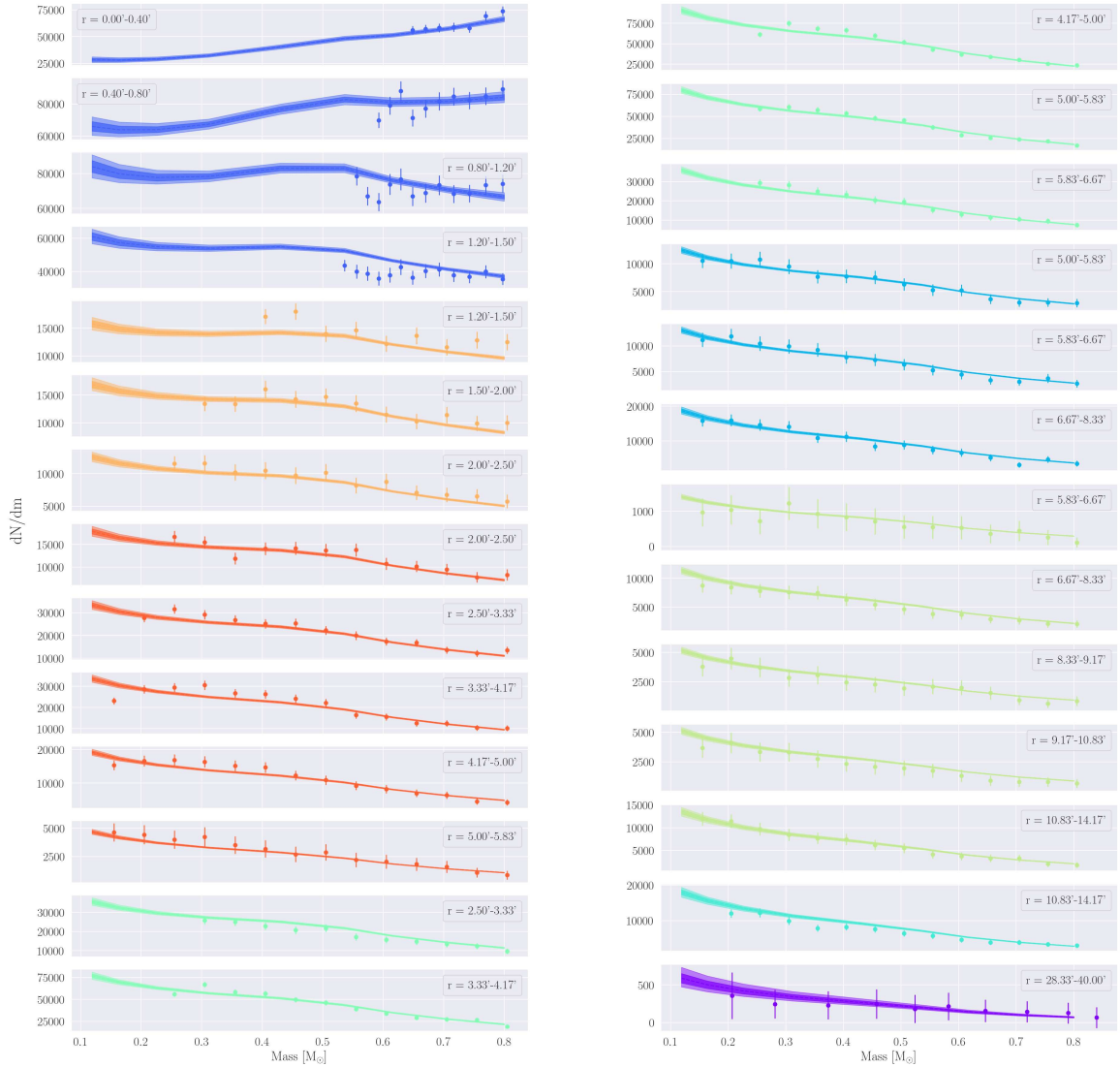


Figure 1.5: The stellar mass function data and model fits for the globular cluster 47 Tuc. Each panel shows the mass function for a different radial region.

The most obvious way that binaries can affect the dynamics of a cluster is through three- or four-body interactions with other cluster members. When a single star (or another binary) interacts with a binary system at a close enough range, if the binary is hard, it will impart some of its energy to the ejected star and “harden” further. If the binary is soft, it will further “soften”, potentially becoming unbound. Through these processes, soft binaries get softer and are slowly disrupted while hard binaries become harder (Heggie, 1975). Hard binary systems can act as a reserve of kinetic energy for a cluster through these three-body interactions with passing cluster members (Heggie & Hut, 2003). Binary stars are thought to be one of the primary mechanisms through which core-collapse (the collapse of the core of a cluster into extremely high density caused by runaway mass segregation) is halted in some clusters by continually adding to the energy of stars which migrate to the central regions, thereby pushing them back out into the extended regions of the cluster (Chatterjee et al., 2013). Because the models that we will be focusing on do not model the evolutionary history of individual objects within the cluster, we will instead focus on the second way that binaries can affect the dynamics of a cluster, as discussed below.

Because binaries are tightly bound, for all interactions except for the very closest, they effectively act as a single point mass equal to the sum of each component’s mass. In this way, binaries can affect cluster dynamics in much the same way that a large population of heavy remnants might. Much like black holes and neutron stars, binary systems will migrate to the centre of a cluster due to the effects of mass segregation. This predicted increase in binary fraction as you get closer to the centre of a cluster is also seen in observations and is illustrated in Figure 1.6 for NGC 3201. It has

been found (e.g. Kremer et al. 2019) that a central population of black holes is typically required in addition to binary systems in order to halt core collapse. Both of these populations slow core collapse by injecting kinetic energy through two-body interactions within the core of the cluster.

The effect of having a significant central population of binaries could be that our mass models are overestimating the number of black holes and other high-mass objects (neutron stars, massive white dwarfs) in the core of the cluster. Because the gravitational potential in the central regions of the cluster is fairly well constrained by kinematic measurements, if we are missing a significant contribution from binaries, the models may be compensating for this “missing mass” by adding more mass to the heavy end of the stellar mass function which would lead to an overestimation of the number of neutron stars and black holes and would have a particularly large impact on the inferred high-mass IMF of globular clusters. By including realistic populations of binary stars in our models, we hope to recover more accurate present-day remnant populations.

### 1.3.2 Observations of Binary Stars in Globular Clusters

In general, there are two methods used to detect binaries within globular clusters: high-precision photometric observations and radial velocity surveys.

High-precision photometry can be used to detect binaries along the main sequence which have a significant difference in the mass of their components. We use the ratio of the mass of the companion star to the mass of the primary star to quantify this

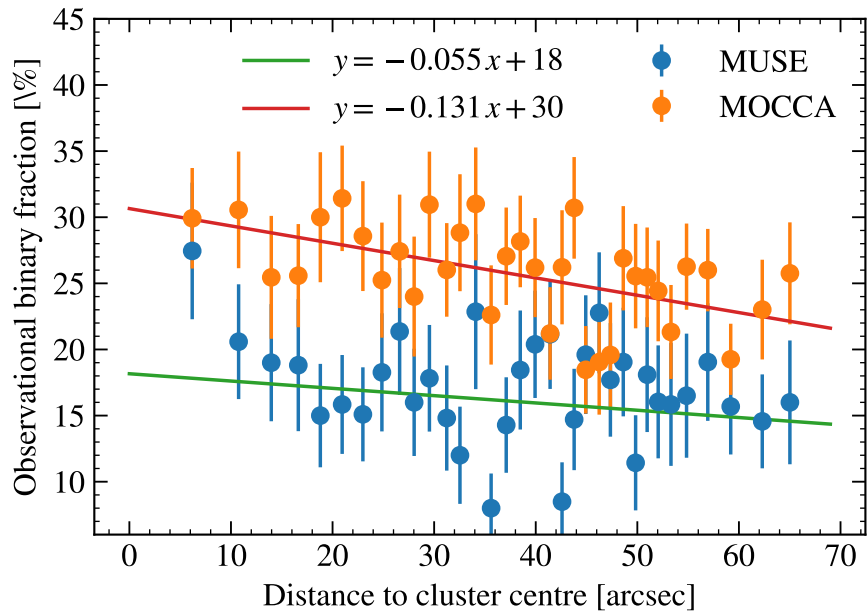


Figure 1.6: Observed binary fraction vs. projected distance from cluster centre for NGC 3201 as inferred from multi-epoch radial velocity measurements from the MUSE instrument. The slight trend in radial binary fraction is visible. Also plotted is the observed binary fraction in a MOCCA model which matches well with NGC 3201. MOCCA is a Monte Carlo code designed to model globular clusters for which there is a large grid of pre-computed models available. Reproduced from Figure 8 of Giesers et al. (2019).

difference: an equal mass binary will have a mass ratio of  $q = 1$  while a binary with a large difference in the masses of its components will have a mass ratio closer to zero. Binaries that are detectable through this method typically have a mass ratio greater than  $q = 0.5$ . These systems will appear to be raised above the main sequence when plotted on a colour-magnitude diagram as their colour will be a combination of the two stars while their luminosity will be the direct sum of each component. Figure 1.7 shows the main sequence of the cluster NGC 2298. The binary stars in this cluster are visible above the main sequence, raised according to their mass ratio. Milone et al. (2012) performed high-precision photometry on several globular clusters using the Hubble Space Telescope’s (HST) Advanced Camera for Surveys and were able to place strong constraints on the binary fraction for binaries with a mass ratio above  $q = 0.5$ . This method allows for large studies of binary populations in GCs without the need for dedicated observations of individual systems but suffers from an inherent bias towards systems with high mass ratios. Systems with mass ratios below  $q = 0.5$  are typically too close to the regular main-sequence to confidently classify as binaries (see Figure 1.7). This means that studies that employ this method must assume an underlying mass-ratio distribution for low values of  $q$  if they wish to place any limits on the overall binary fraction of a cluster. Typical values for the binary fraction in massive clusters found using this method range from almost zero to an upper limit of around 15% (Milone et al., 2012). Additionally, studies of the mass ratio distribution within these clusters using the same method find a preference for a uniform or “flat” distribution unlike the distribution in the solar neighbourhood which is peaked at  $q = 1.0$  (Milone et al., 2012; Fisher et al., 2005; Reggiani & Meyer, 2013)

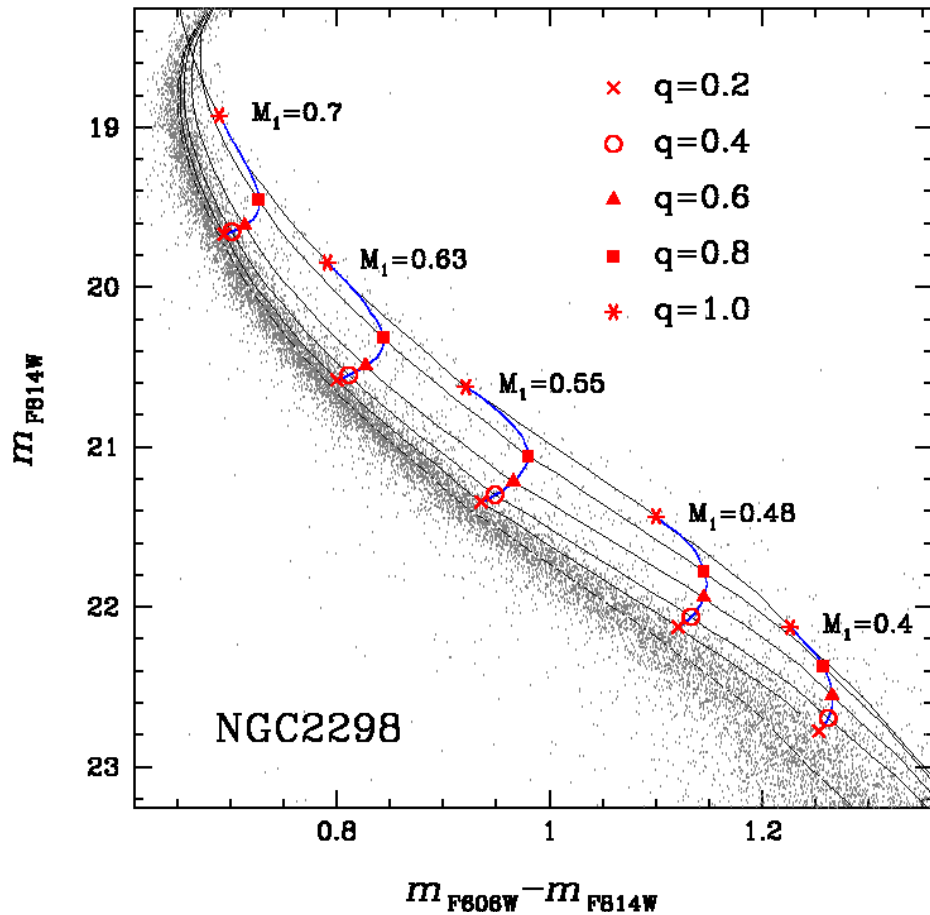


Figure 1.7: The main-sequence portion of the colour-magnitude diagram for NGC 2298. Binary systems are visible as being raised above the primary main sequence with systems with a higher mass ratio being raised further off of the main sequence. Systems below a mass ratio of  $q = 0.5$  are nearly indistinguishable from the regular spread in main sequence stars. Reproduced from Figure 1 of Milone et al. (2012).

Large-scale campaigns to measure the radial velocities for many stars in a cluster over many epochs are another method that can be used to detect binaries in GCs. Systems that are found to have periodically varying radial velocities can typically be confidently classified as binary systems. Giesers et al. (2019) used the MUSE integral field spectrograph installed at the European Southern Observatory’s Very Large Telescope to observe several GCs and reported the results for NGC 3201. Integral field spectrographs provide spatially resolved spectra for the entire field of view of the detector which enables far more time-efficient surveys than previous methods. Because this method measures radial velocities over time, periods for the binaries can be accurately determined and given enough measurements, many other parameters like eccentricity and companion mass can be accurately constrained in contrast to photometric methods which can only provide the mass ratio. This method also suffers from biases in that it requires the binary system to be bright enough to enable good spectroscopic measurements which may bias the sample towards systems with more massive stars. For NGC 3201, the binary fraction found using this method was  $6.75 \pm 0.72\%$  (Giesers et al., 2019) which differs from the photometric estimates of Milone et al. (2012) which range from 10-12% for different fields due to the different selection effects in each study.

## 1.4 This Thesis

To summarize, binary systems are an ingredient that is lacking from our current distribution-function based models. In this thesis we will develop a method to in-

clude binaries in the LIMEPY models and use this method to investigate the dynamical effects of the binaries. We will be focusing primarily on the interplay between the binary content of a cluster and its remnant population, in particular, how binaries can fill the role of heavy remnants in the overall mass distribution of the cluster. The remainder of the thesis is structured as follows: Chapter 2 describes the method used to generate mass functions which include realistic binary populations as well as the specifics of fitting these modified mass functions to real observations of stellar mass functions. Chapter 3 discusses the results of the model fits. Chapter 4 discusses the differences between models with and without binaries as well as the overall implications of including binaries in our models, specifically when fitting them to observations. Chapter 5 summarizes our findings and discusses future work.

# Chapter 2

## Methods

### 2.1 Data

We use a wide range of data to constrain the parameters of our models. In general, we use archival kinematic data from ground-based spectroscopy, proper motions from HST and *Gaia*, number density profiles from *Gaia* supplemented with archival data, stellar mass function data from HST photometry and pulsar timing data.

#### 2.1.1 Kinematics and density profiles

##### Proper motion dispersion profiles

We use two sets of *Hubble Space Telescope* (HST) proper motion data. To probe the inner regions of the cluster we use the proper motion dispersion profiles (both tangential and radial components) from Watkins et al. (2015) which are based on a catalogue of proper motions of bright stars from Bellini et al. (2014). These dispersion profiles are built from stars brighter than the main sequence turn-off (around  $0.85 M_{\odot}$  for 47 Tuc). To probe the kinematics in the outer regions of the cluster, we also use the data from Heyl et al. (2017), for which the mean mass of the measured stars is  $0.38 M_{\odot}$ . The outer proper motion data also allows us to constrain the amount of radial anisotropy present in the cluster, which can mimic the effect of central dark

mass in isotropic models by raising the central velocity dispersion (Zocchi et al., 2017).

### Line-of-sight velocity dispersion profiles

We use the line-of-sight velocity dispersion profile from Baumgardt & Hilker (2018) to further constrain the kinematics of the cluster. The dispersion profile is based on archival ESO/VLT and Keck spectra along with previously published radial velocity data from the literature. As these radial velocity samples are dominated by bright stars, we assume that the velocity dispersion profile traces the kinematics of upper main-sequence and evolved stars in our models.

### Number density profiles

We use the number density profile from De Boer et al. (2019) to constrain the size and structural parameters of the cluster. These profiles are made up of a combination of cluster members based on Gaia DR2 data in the outer regions and surface brightness data from Trager et al. (1995) in the central regions. The Gaia data only includes bright stars ( $m > 0.6 M_{\odot}$ , for both clusters) and the literature data is also dominated by bright stars, therefore in our models we assume the profiles probe the spatial distribution of upper main sequence and evolved stars.

#### 2.1.2 Stellar mass functions

As a constraint on the global present-day stellar mass function of the cluster, we use a compilation of HST-based stellar mass function data from Baumgardt<sup>1</sup> (2021,

---

<sup>1</sup><https://people.smp.uq.edu.au/HolgerBaumgardt/globular/>

priv. comm.), which represent an updated and augmented version of the stellar mass functions found in Sollima & Baumgardt (2017). This compilation is made up of several HST fields at varying distances from the cluster centre. These fields extend out to  $14'$  from the cluster centre and cover a mass range of  $0.16 - 0.8 M_{\odot}$ . The large radial and mass ranges allow us to constrain the change of the local stellar mass function with distance from the cluster centre and therefore the degree mass segregation in the cluster.

### 2.1.3 Pulsar Data

We make use of the large population of millisecond pulsars (MSPs) in 47 Tuc to place further constraints on its mass distribution. We use timing solutions from Freire et al. (2017), Ridolfi et al. (2016) and Freire & Ridolfi (2018) which include both the spin and orbital periods. We also consider the dispersion measures of the pulsars which is a measure of how much gas the signal has passed through on its way to the observer. When combined with internal gas models from Abbate et al. (2018), the dispersion measures allow us to constrain the line-of-sight position of the pulsars within the cluster. The pulsar data is summarized in Tables A.1 and A.2.

## 2.2 Binary Fraction Measurements

In order to create realistic binary populations we refer to the measurements of Milone et al. (2012) to inform our choices of binary fraction and mass ratio distribution. For 47 Tuc this means a flat mass ratio distribution and a binary fraction of roughly 2%

where the binary fraction is defined as the ratio between binary systems and total systems (Equation 2.1). Because this estimate of the binary fraction is so small, we will use it as a lower limit for the binary fraction and also test a case where the binary fraction is around 10%, representing a case where the binary fraction is significant.

$$f_b = \frac{N_{bin}}{N_{bin} + N_{single}} \quad (2.1)$$

## 2.3 Generating mass functions

An important part of this thesis deals with generating mass functions to use as inputs to the `LIMEPY` models. We do this in two main steps, we first generate a present-day mass function comprised of only single stars, and we then modify it to include binary stars.

### 2.3.1 Single Star Mass Functions

To generate the mass functions comprised of single stars we use the `evolve_mf` algorithm from `SSPTools`<sup>2</sup> (first presented in Balbinot & Gieles 2018), a publicly available package for working with simple stellar populations. As part of the previous project, we updated `evolve_mf` to include realistic prescriptions for the BH mass function by including the effects of natal kicks in addition to dynamical ejections.

The `evolve_mf` algorithm combines precomputed grids of stellar evolution models, isochrones and initial-final mass relations to accurately model the evolution of a given

---

<sup>2</sup>[www.github.com/pjs902/ssptools](https://www.github.com/pjs902/ssptools)

---

initial mass function, including the effects of stellar evolution as well as mass loss due to escaping stars and dynamical ejections. The algorithm returns a binned mass function at a requested evolutionary time, ideal for use as an input in the LIMEPY models.

We parameterize the mass function as a broken power-law with breakpoints at  $0.5 M_{\odot}$  and  $1.0 M_{\odot}$ . We provide to `evolve_mf` the initial mass function slopes ( $\alpha_1$ ,  $\alpha_2$  and  $\alpha_3$ ) and breakpoints, the cluster age, metallicity and escape velocity, as well as parameters which control the mass loss due to escaping stars and the specific binning to be used when returning the final discrete mass-function bins. We finally provide the black hole retention fraction ( $BH_{ret}$ ) which controls how many of the black holes created from the IMF are retained to the present day. For this study we do not model the mass loss due to tidal stripping, so we set the mass loss due to escaping stars to be zero, and we are effectively specifying the present day mass function for low-mass stars. Figure 2.1 shows the evolution of a mass function over a span of 10 Gyr (VandenBerg et al. 2013 found the age of 47 Tuc to be 11.75 Gyr).

### 2.3.2 Binary Mass Functions

In order to include binary stars in our mass functions we make use of the assumption that for the vast majority of their interactions with other objects, binary systems behave essentially as point masses due to the fact that they are tightly bound. This means that in order to replicate the effects of a binary population in our mass function, we simply need to shift some of the mass in single stars into heavier bins which act

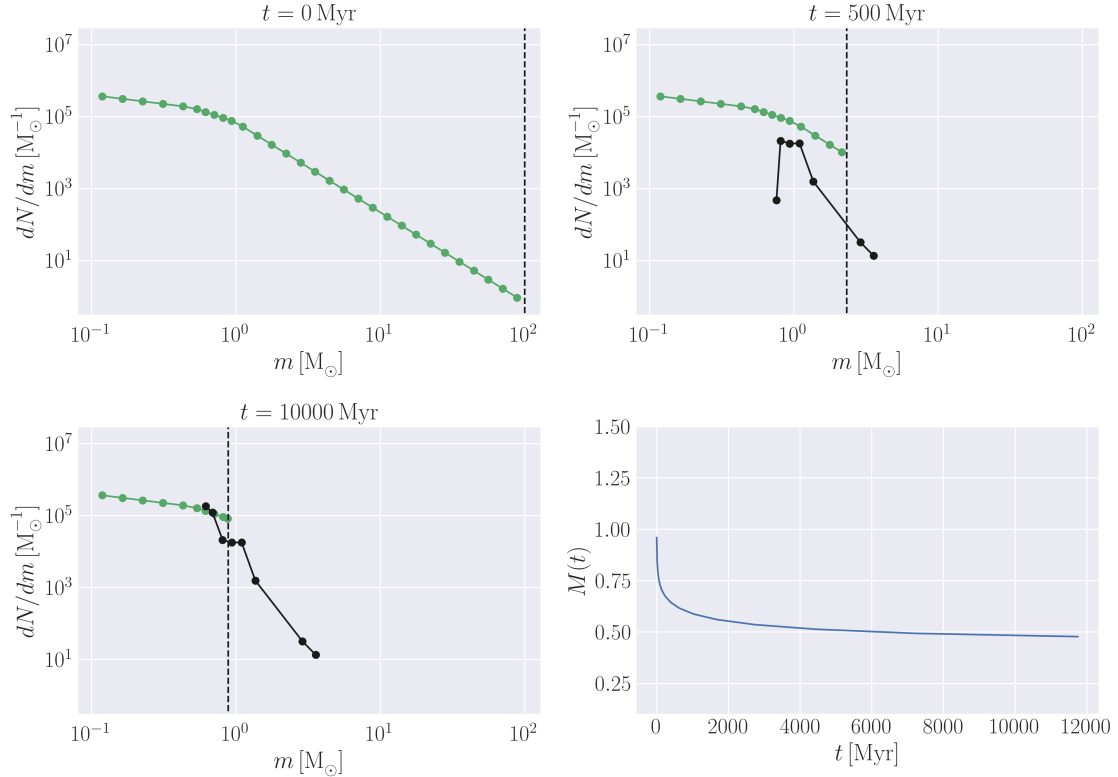


Figure 2.1: The evolution of a typical mass function from  $t = 0$  to  $t = 10$  Gyr. The stellar bins are plotted in green while the remnant bins are plotted in black, the current main-sequence turn-off is plotted as a dashed black line. As the cluster ages, more and more main sequence stars evolve into remnants. The lack of mass loss in the low-mass regime is evident, we set the mass loss due to escaping stars to be zero, meaning that we are effectively fitting on the present-day mass function for low-mass stars. Lower right: The evolution of the total mass of the cluster is plotted as a fraction of the initial mass. Mass loss is dominated by the effects of stellar evolution but also has contributions from ejected heavy remnants.

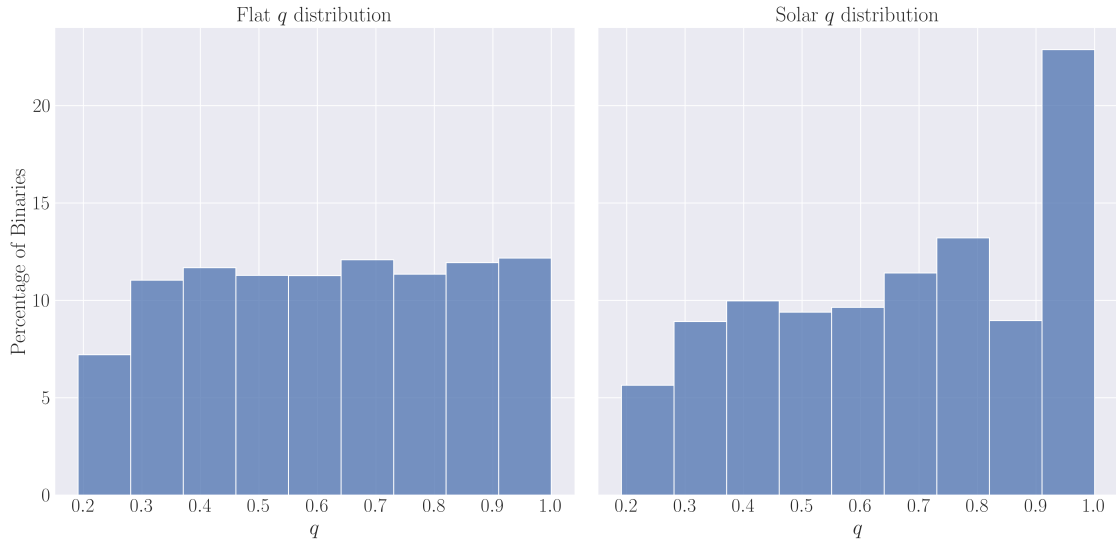


Figure 2.2: The resulting mass ratio distributions for the “flat” and “solar” mass ratio distributions. Both distributions are truncated and lowered at  $q = 0.2$  due to the relative lack of low very low mass stars within the mass functions, making the creation of binary systems with a very low mass ratio impossible.

as the “binary bins”.

We split this process up into several steps. First, we assign a portion of the total binary fraction to each value of  $q$  in the requested mass ratio distribution. We weight the  $f_b$  values assigned to the individual values of  $q$  by the chosen mass ratio distribution. A flat mass ratio distribution would have the total binary fraction split evenly among the values, while a “solar distribution” (see Reggiani & Meyer 2013) would have a significantly higher number of equal-mass binaries compared to a flat distribution. Figure 2.2 shows the resulting mass ratio distributions using this method.

After we have assigned a portion of the total binary fraction to each value of  $q$ , we then go through each bin of main-sequence stars to make binaries. The companion

mass for a given bin is calculated for each value of  $q$  in the mass ratio distribution and the number of binaries to make is calculated using the portion of the binary fraction assigned to each value of  $q$ . After the companion mass and number of binaries are set, we then remove mass from the primary bin and the bin that most closely matches the mass of the companion and add the mass to a new bin with a mean mass equal to the sum of the primary and companion masses. Through this process we move mass between bins of differing *mean* masses while conserving the *total* mass in stars in the model.

We repeat this process for each bin of main-sequence stars until each bin has a binary fraction equal to the total requested binary fraction and a mass ratio distribution identical to the requested distribution, this results in the overall binary fraction and mass ratio distribution for the cluster matching the requested values.

This process tends to create on the order of 150 new bins in our mass function which dramatically increases the runtime of the LIMEPY models. In order to prevent this, we group together binary bins of similar masses, forming 15 “binary bins” containing binary systems of similar total mass but differing mass ratios. Figure 2.3 shows the original main sequence bins, plotted with the modified main sequence bins, binary bins and rebinned binary bins.

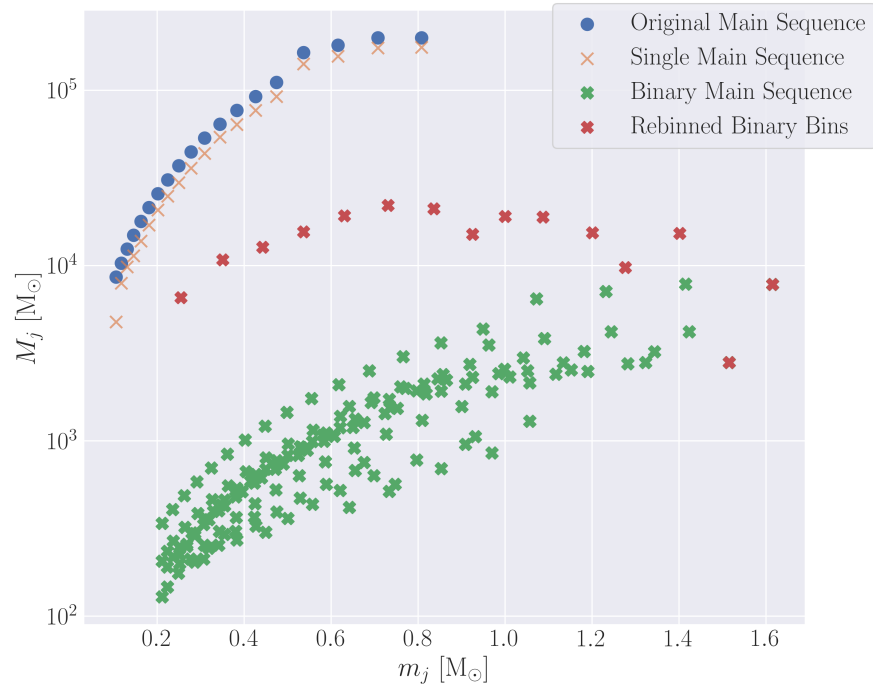


Figure 2.3: The main-sequence portion of a mass function before and after binaries are added.  $M_j$  is the total mass within a bin while  $m_j$  is the mean mass of the bin. The blue circles are the original main sequence bins and the crosses are the modified main sequence bins. The orange crosses show the single stars after mass has been removed to create binaries and the many green crosses are the binary bins that are initially created. The red crosses are the rebinned binary bins which are actually used in the computation of the LIMEPY models.

## 2.4 Fitting Models to Data

To fit our models to the data we use the `GCfit` package<sup>3</sup>. `GCfit` provides a uniform interface for fitting `evolve_mf` and `LIMEPY` models to observations of clusters using either MCMC or Nested Sampling.

For this project we use the MCMC backend which is powered by `emcee` Foreman-Mackey et al. (2013, 2019), an affine-invariant ensemble sampler. We use 1024 walkers, initialized at a small randomized sphere around a reasonable initial guess for the model parameters. The parameters and their priors are summarized in Table 2.1. We run the chains for 2500 steps and discard the initial 2000 steps as the burn-in period. Trace and corner (Foreman-Mackey, 2016) plots for all three chains are shown in Figures A.4 through A.9.

### 2.4.1 Likelihoods

The majority of the likelihood functions we use are simple Gaussian likelihoods. Provided below is the likelihood for velocity dispersion profile data and all other likelihoods are of a similar form:

$$\ln(\mathcal{L}) = \frac{1}{2} \sum_r \left( \frac{(\sigma_{\text{obs}}(r) - \sigma_{\text{model}}(r))^2}{\delta\sigma_{\text{obs}}^2(r)} - \ln(\delta\sigma_{\text{obs}}^2(r)) \right) \quad (2.2)$$

Where  $\mathcal{L}$  is the likelihood,  $\sigma$  is the line-of-sight velocity dispersion,  $r$  is the projected distance from the cluster centre, and  $\delta\sigma$  is the uncertainty in the velocity dispersion. The likelihoods for other observables are formulated in the same way,

---

<sup>3</sup>[www.github.com/nmdickson/gcfit](https://www.github.com/nmdickson/gcfit)

Table 2.1: Model parameters and their priors. Most priors are uniform and are chosen to bound the chains around a reasonable range of parameter values for 47 Tuc. For the mass function slopes we add the additional constraint that  $\alpha_2$  must be steeper than  $\alpha_1$  and  $\alpha_3$  steeper than  $\alpha_2$  to ensure that we are only testing mass functions that make sense physically. For the distance we use a Gaussian prior with the distance measurement from Baumgardt & Vasiliev (2021) providing the mean and standard deviation of the prior.

Parameter	Prior
$W_0$	Uniform (4, 10)
$M(10^6 M_\odot)$	Uniform (0.1, 1.5)
$r_h(\text{pc})$	Uniform (0.5, 10)
$\log_{10} r_a/\text{pc}$	Uniform (0, 5)
$g$	Uniform (0, 2.3)
$\delta$	Uniform (0.3, 0.5)
$s^2$	Uniform (0, 15)
$F$	Uniform (1, 5)
$\alpha_1$	Uniform (0, 2.35)
$\alpha_2$	Uniform (0, 2.35) and $\geq \alpha_1$
$\alpha_3$	Uniform (1.6, 4) and $\geq \alpha_2$
$BH_{ret}(\%)$	Uniform (0, 5)
$d(\text{kpc})$	Gaussian ( $4.521 \pm 0.031$ )

and the specifics are discussed in `GCfit`'s documentation<sup>4</sup>. The total log-likelihood is therefore the sum of all the log-likelihoods for each set of observations.

For the mass function and number density profile likelihoods we include additional nuisance parameters and scaling terms.

In the case of the number density data we introduce a parameter  $s^2$  which is added in quadrature to the existing measurement uncertainties. This parameter allows us to add a constant amount of uncertainty to all values in the data-set, effectively assigning less significance to the data located furthest from the cluster centre where the number density is lowest. This allows us to account for both background effects on the observations as well as for any effects that may be present near the cluster

---

<sup>4</sup>[gcfit.readthedocs.io](https://gcfit.readthedocs.io)

boundary that the LIMEPY models do not account for such as the effects of potential escapers (see Claydon et al. 2019 for a discussion of potential escapers in equilibrium models).

For the mass function data the only uncertainty included with the data is the Poisson counting error. We introduce the nuisance parameter  $F$  which is defined as a factor between 1 and 5 by which we adjust each data point's absolute error. This error encapsulates additional sources of error that may not have been accounted for as well as addresses the fact that the mass function is being approximated as a broken power-law.

## Pulsar Likelihood

As stated previously, the development of a method to use pulsar acceleration measurements to constrain the models was performed as part of an earlier project, but we provide a description of the process below.

Pulsar period derivatives, as measured by an observer, are made up of several distinct components, only one of which is related to the cluster potential. The effects of the proper motion of the pulsar and the galactic potential of the pulsar are fairly easily constrained based on the pulsar's position in the galaxy but, the effects of processes like magnetic breaking or accretion are not. Equation 2.3 shows the breakdown of the measured period derivative into separate components where  $(\dot{P}/P)_{int}$  is any change in period due to the effects intrinsic to the pulsar like magnetic breaking or accretion,  $a_c$  is the change due to the cluster's gravitational potential and is the quantity we are interested in,  $a_g$  is the effect of the galaxy's gravitational potential

and is easily adjusted for based on 47 Tuc’s position within the Milky Way,  $a_s$  is the effect of the pulsar’s proper motion and is similarly easy to compensate for,  $a_{DM}$  is the effect of the changing dispersion measure between the pulsar and the observer and is a minor effect which we assume is well compensated for in our treatment of the intrinsic period derivative.

$$\left(\frac{\dot{P}}{P}\right)_{meas} = \left(\frac{\dot{P}}{P}\right)_{int} + \frac{a_c}{c} + \frac{a_g}{c} + \frac{a_s}{c} + \frac{a_{DM}}{c} \quad (2.3)$$

In order to constrain the 3D position of the pulsars within the cluster we adopt a model for the internal gas distribution of the cluster from Abbate et al. (2018). We adopt their best fitting model which is a uniform distribution of ionized gas with a number density of  $n_g = 0.23 \pm 0.05 \text{ cm}^{-3}$ . We also adopt their estimate for the total dispersion measure between the observer and the cluster centre:  $DM_c = 24.38 \pm 0.02 \text{ pc cm}^{-3}$ . By adopting a model for the gas distribution, we are able to accurately determine the pulsars line-of-sight position ( $l$ ) within the cluster using the following equation (Equation 28 in Abbate et al. (2018)):

$$DM = n_g l + DM_c \quad (2.4)$$

Combining the accurate estimate of  $l$  with the well-measured projected distance from the cluster centre allows us to very accurately determine the pulsar’s 3D position within the cluster.

In order to assign a likelihood to a particular  $\dot{P}/P$  measurement we first use the LIMEPY models to generate a line-of-sight acceleration profile for the given model.

We then use this acceleration profile to interpolate the possible line-of-sight positions for the pulsar. These line-of-sight positions are then assigned a probability based on a Gaussian centred at the line-of-sight position as calculated from the DM with a dispersion equal to the uncertainty of the DM-based line-of-sight position. The likelihood is the sum of the probabilities at each of the interpolated line-of-sight positions from the model.

For pulsars that are not consistent with the uniform gas model (pulsars AA and D, see Abbate et al. 2018 for details) we instead assign a probability distribution to the line-of-sight position based on the model density of pulsar-mass objects at the given line of sight. These constraints are less precise than the DM-based constraints but allow us to use pulsars that are not well-fit by a uniform gas distribution to constrain the properties of the cluster.

To constrain intrinsic spin-down of the pulsars, we assume the spin-down to be identical to pulsars found in the galaxy, outside of clusters, and dependant only on their period. The field pulsars, as they are unaffected by the cluster potential, can have their intrinsic spin-down determined directly. A Gaussian kernel density estimator is computed in the field  $P-\dot{P}$  space, which is sliced along each cluster pulsar's period to extract a distribution of possible intrinsic values. This distribution of intrinsic spin-down values is then convolved with the probability distribution from the model.

A resulting probability distribution from this method is shown in Figure 2.4, while figures A.1 through A.3 show the agreement between best-fitting models and the period derivates for both orbital and spin periods.

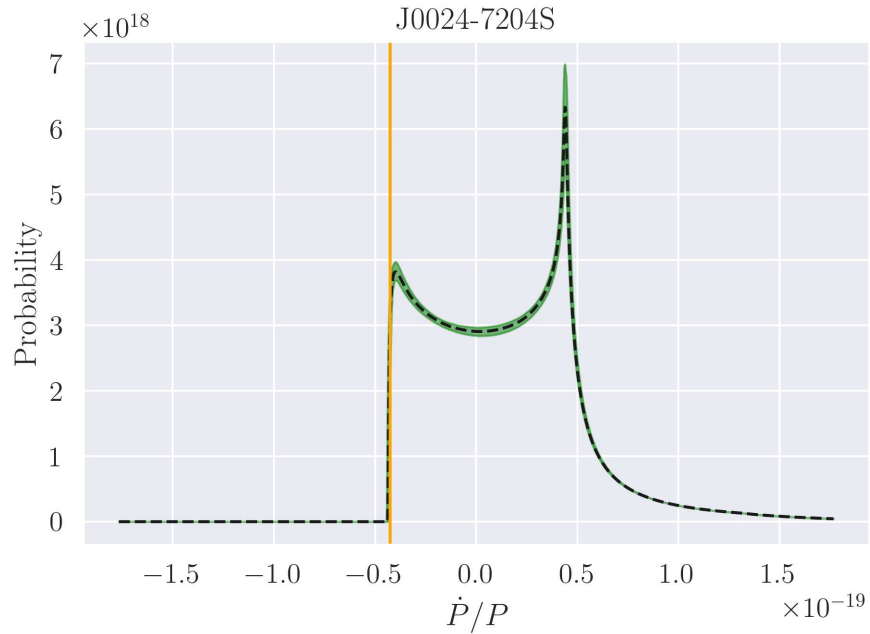


Figure 2.4: The resulting probability distribution for the spin period derivative of pulsar 47 Tuc S from the method described above for the best-fitting models of 47 Tuc. The green line is the likelihood of a given period derivative measurement given the best-fitting model parameters and the yellow line is the measured spin period derivative. The asymmetry in the distribution is due to the intrinsic spin-down of the pulsar, biasing the distribution to positive values of  $\dot{P}/P$ .

Many of the pulsars in 47 Tuc are in binary systems and for 10 of these systems we have timing solutions for the binary system. These binary periods are useful because they are on the order of days rather than milliseconds. This means that the intrinsic effects that affect the spin periods are negligible and any measured change in the period can be entirely attributed to the acceleration from the cluster. Due to the much longer period, the number of detections is greatly reduced resulting in a much larger uncertainty than the spin period derivatives. This large uncertainty means the likelihood distributions for orbital period derivatives are wider and are not suited for placing hard constraints on the mass distribution of the cluster, we nonetheless use the orbital periods of these systems as an additional constraint on the cluster potential.

### 2.4.2 Fitting Mass Functions to Observations

When the mass function data was originally extracted, the mass was inferred based on the position of the star on an isochrone fit to the cluster colour-magnitude diagram (see Sollima & Baumgardt 2017 for details). This means that any binary stars in the observed sample are interpreted as single stars with a mass corresponding to a star with the combined colour of the two binary components and a luminosity corresponding to the sum of the two components. When comparing our models to the data, we want to extract the mass function profiles in the same way that the data was collected.

Additionally, when we move mass around to create binary bins in our models, we

also affect the surface density profiles which are used to compute the mass function profiles. In order to compensate for these effects, we rescale the main-sequence surface density profiles to include the stars which are in binary bins, according to the mass they would have been assigned using the observational method described above, which assumed that all stars are single.

In order to determine the “observed” mass we use a grid of MIST isochrones (Dotter, 2016; Choi et al., 2016)<sup>5</sup> computed at a range of metallicities, at the age of the cluster. We use the isochrone closest to the model parameters (an age of 11.75 Gyr, Fe/H of -0.75, and we assume no stellar rotation) to determine the luminosity of the binary components and then again use the isochrone to determine the observed mass of the combined luminosities. Figure 2.5 shows the derived relation between stellar mass and luminosity used for these conversions. After having determined the mass that would have been inferred for a binary system if it was assumed to be a single star, we then scale the surface density profile of the main-sequence bin which most closely matches the “observed” mass of the binary system to include the total mass of the binary system which allows us to correct for both effects.

---

<sup>5</sup>We use the EZMIST library to fetch and prepare the isochrones. EZMIST is available online: <https://github.com/mfouesneau/ezmist>

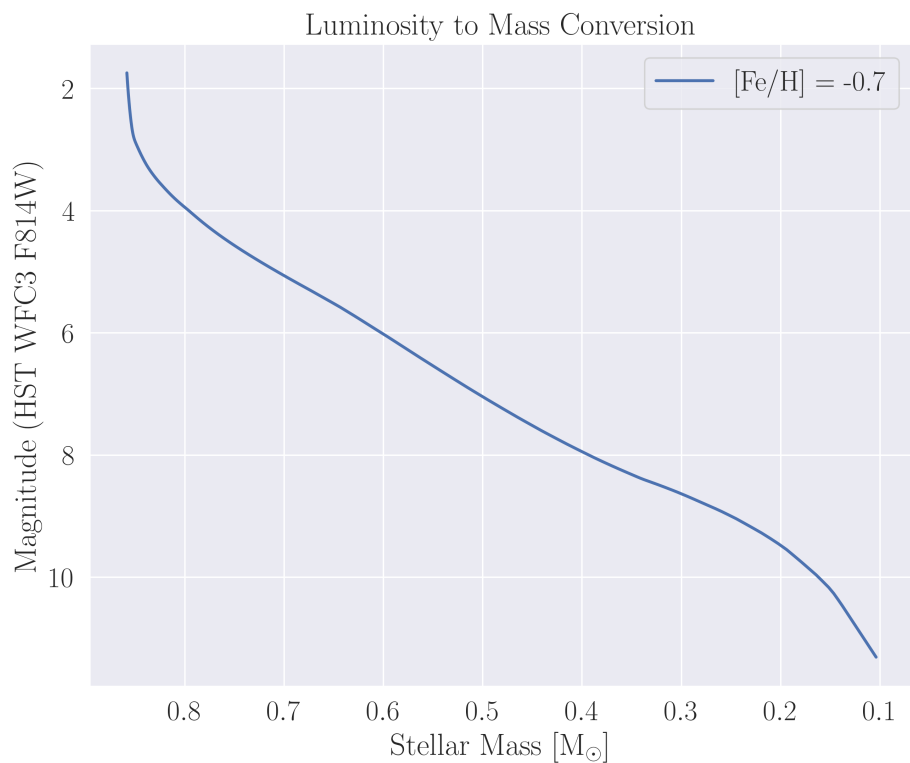


Figure 2.5: Relation between stellar mass and luminosity through HST/WFC3's F814W filter, derived from a MIST isochrone. The F814W filter is used to replicate the original observations, see Sollima & Baumgardt (2017) for further details.

# Chapter 3

# Results

## 3.1 Previous Results

As mentioned previously, this thesis is a continuation of a project done over the previous year in which we developed a method to use pulsar timing data to constrain our mass models of the globular cluster 47 Tuc. The final results of that project were a set of models that accurately reproduce all observables and fully incorporated the pulsar data in the likelihood. Figure A.10 shows the model fits to most of the observables while Figure A.11 shows the fit to the stellar mass function data. In both cases, the model satisfactorily reproduces all observables. The median and  $1\sigma$  credibility intervals of the best-fit parameters are listed in Table 3.1.

One of the most interesting results of the previous project was the model's ability to constrain the black hole content within 47 Tuc. Figure 3.1 shows the distribution of mass in black hole mass and number of black holes in our set of best-fit models, which were found to be  $135^{+104}_{-92} M_{\odot}$  and  $26^{+15}_{-15}$  black holes respectively. Both the total mass and number are quite well contained especially in comparison to the previous constraints in the literature (see e.g. Hénault-Brunet et al., 2020; Weatherford et al., 2020).

Table 3.1: Best-fit parameters with  $1\sigma$  credibility intervals for models with a binary fraction of 0%.

Parameter	Value
$W_0$	$6.26^{+0.11}_{-0.10}$
$M/10^6 M_\odot$	$0.88^{+0.01}_{-0.01}$
$r_h/pc$	$6.73^{+0.06}_{-0.06}$
$\log_{10} r_a/pc$	$1.50^{+0.07}_{-0.05}$
$g$	$1.37^{+0.06}_{-0.06}$
$\delta$	$0.43^{+0.02}_{-0.02}$
$s^2$	$0.01^{+0.01}_{-0.00}$
$F$	$3.25^{+0.14}_{-0.12}$
$\alpha_1$	$0.35^{+0.02}_{-0.02}$
$\alpha_2$	$1.46^{+0.05}_{-0.05}$
$\alpha_3$	$2.13^{+0.04}_{-0.04}$
$BH_{ret}(\%)$	$0.07^{+0.06}_{-0.04}$
$d$	$4.42^{+0.02}_{-0.02}$

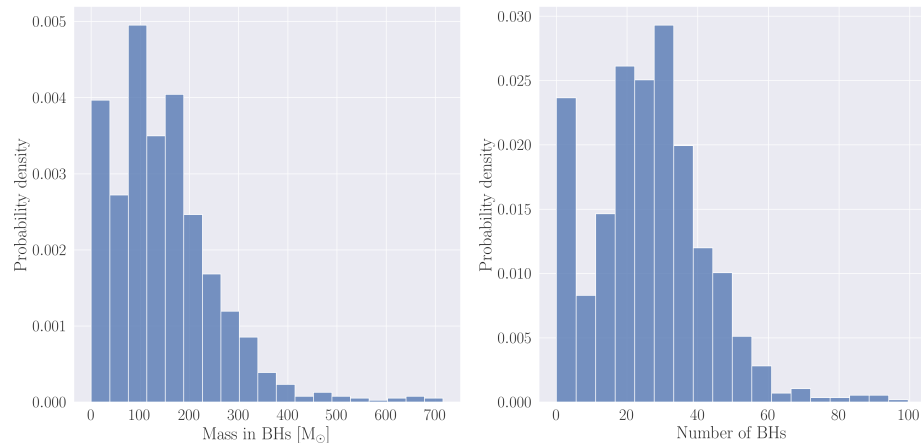


Figure 3.1: Distribution in mass and number of black holes for models with a 0% binary fraction.

Table 3.2: Best-fit parameters with  $1\sigma$  credibility intervals for models with a 2% binary fraction.

Parameter	Value
$W_0$	$6.28^{+0.10}_{-0.10}$
$M/10^6 M_\odot$	$0.89^{+0.01}_{-0.01}$
$r_h/pc$	$6.74^{+0.06}_{-0.06}$
$\log_{10} r_a/pc$	$1.50^{+0.06}_{-0.05}$
$g$	$1.36^{+0.06}_{-0.06}$
$\delta$	$0.43^{+0.02}_{-0.02}$
$s^2$	$0.01^{+0.01}_{-0.00}$
$F$	$3.24^{+0.13}_{-0.12}$
$\alpha_1$	$0.37^{+0.02}_{-0.02}$
$\alpha_2$	$1.47^{+0.05}_{-0.05}$
$\alpha_3$	$2.18^{+0.04}_{-0.04}$
$BH_{ret}(\%)$	$0.08^{+0.09}_{-0.05}$
$d$	$4.42^{+0.02}_{-0.02}$

## 3.2 Low Binary Fraction

In the models with a 2% binary fraction, we find a similar ability to reproduce all the observables, Figure 3.2 and Figure 3.3 show the model fits compared to the data.

The black hole content in these models is also quite well contained, though different from the models without binaries. Figure 3.4 shows the distribution of mass in black holes and number of black holes which this time, are found to be  $22^{+13}_{-19}$  black holes or  $114^{+144}_{-79} M_\odot$  in black holes. The best-fit parameters and the  $1\sigma$  credibility intervals for this set of models are listed in Table 3.2.

A binary fraction of 2% results in a total mass in binaries of around  $15800 M_\odot$ , Figure 3.5 shows the distribution of mass in binaries in our set of best-fitting models.

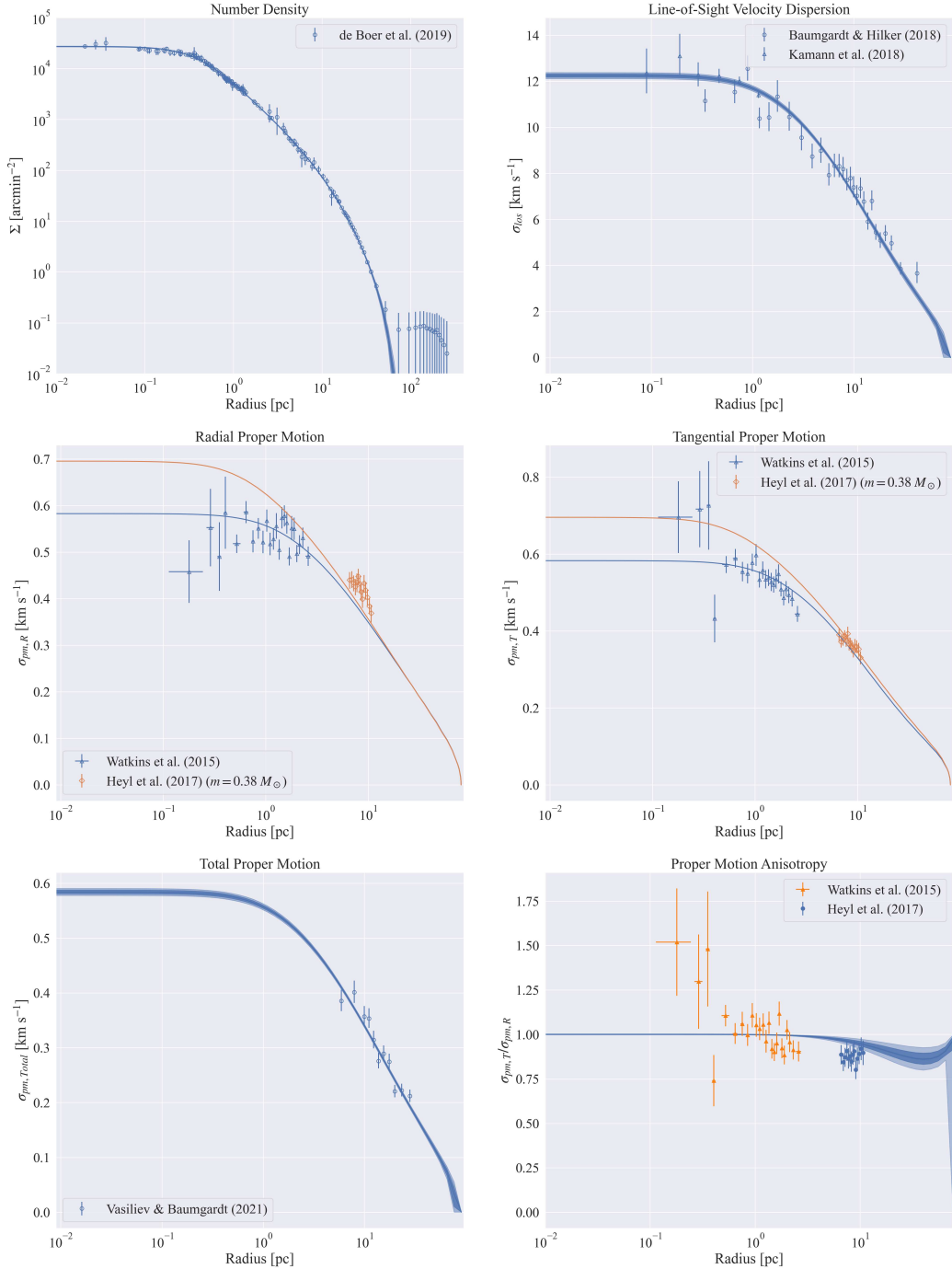


Figure 3.2: Model fits to observables for models with a 2% binary fraction.

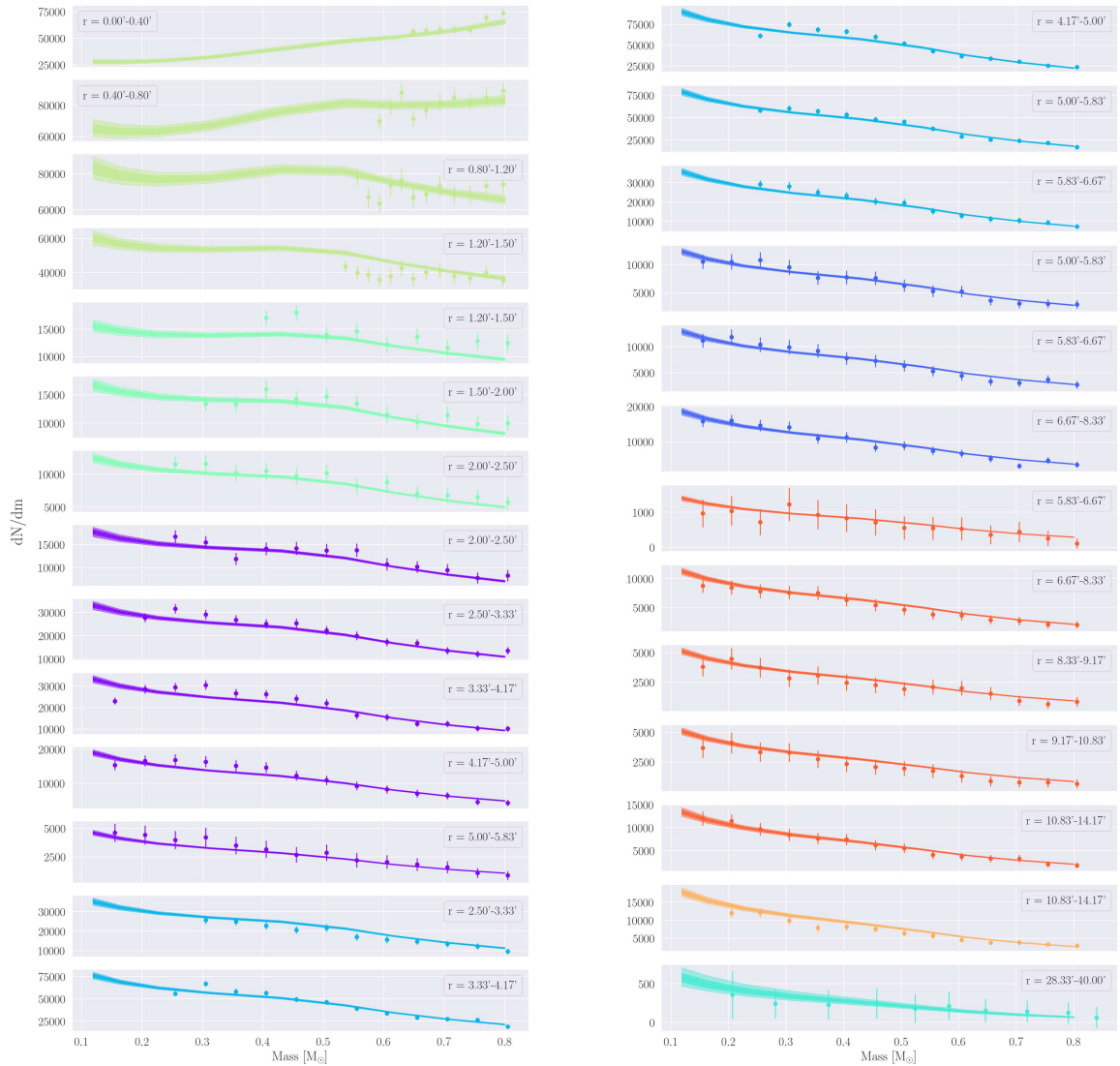


Figure 3.3: Model fits to stellar mass function data for models with a 2% binary fraction.

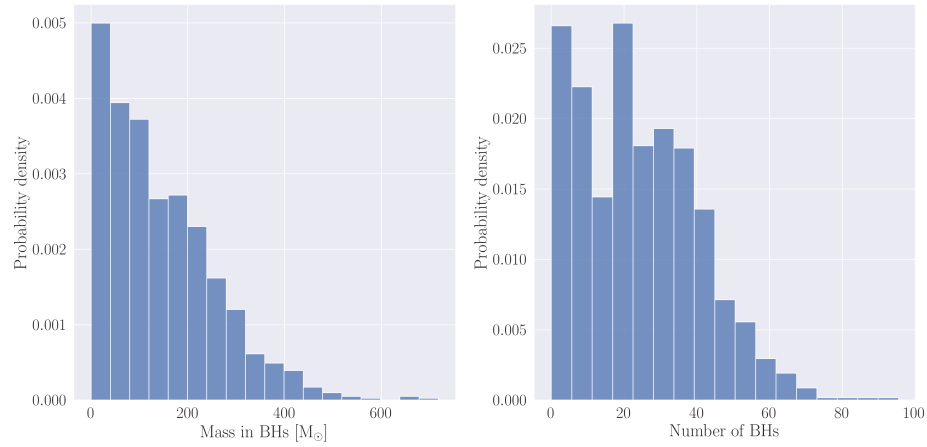


Figure 3.4: Distribution in mass and number of black holes for models with a 2% binary fraction.

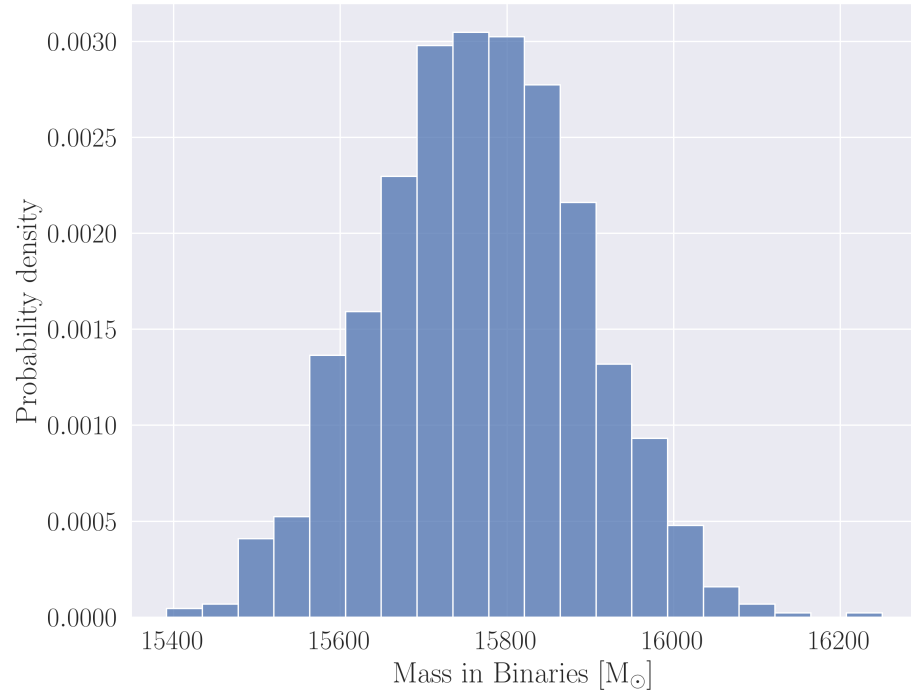


Figure 3.5: Distribution of mass in binaries for models with a 2% binary fraction.

Table 3.3: Best-fit parameters with  $1\sigma$  credibility intervals for models with a 10% binary fraction.

Parameter	Value
$W_0$	$6.36^{+0.09}_{-0.09}$
$M/10^6 M_\odot$	$0.89^{+0.01}_{-0.01}$
$r_h/pc$	$6.77^{+0.06}_{-0.06}$
$\log_{10} r_a/pc$	$1.48^{+0.06}_{-0.05}$
$g$	$1.34^{+0.06}_{-0.06}$
$\delta$	$0.41^{+0.01}_{-0.01}$
$s^2$	$0.01^{+0.01}_{-0.00}$
$F$	$3.16^{+0.13}_{-0.12}$
$\alpha_1$	$0.45^{+0.02}_{-0.02}$
$\alpha_2$	$1.53^{+0.05}_{-0.04}$
$\alpha_3$	$2.46^{+0.05}_{-0.05}$
$BH_{ret}(\%)$	$0.17^{+0.18}_{-0.12}$
$d$	$4.43^{+0.02}_{-0.02}$

### 3.3 High Binary Fraction

As is the case for the models with a low binary fraction, the models with a 10% binary fraction fit the observables very well. Figures A.12 and A.13 show the model fits compared to the data.

With a higher binary fraction, we now find fewer black holes, Figure 3.6 shows the distribution in mass and number which are found to be  $12^{+13}_{-12}$  black holes or  $81^{+121}_{-81} M_\odot$  in black holes.

With a 10% binary fraction we now have a significant amount of mass in binaries, roughly  $81000 M_\odot$  (see figure 3.7), which is a bit less than 2% of the total cluster mass.

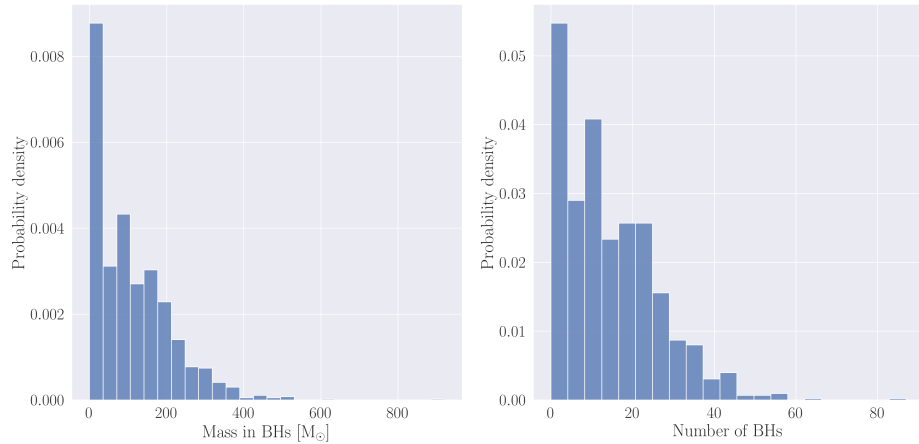


Figure 3.6: Distribution in mass and number for models with a 10% binary fraction.

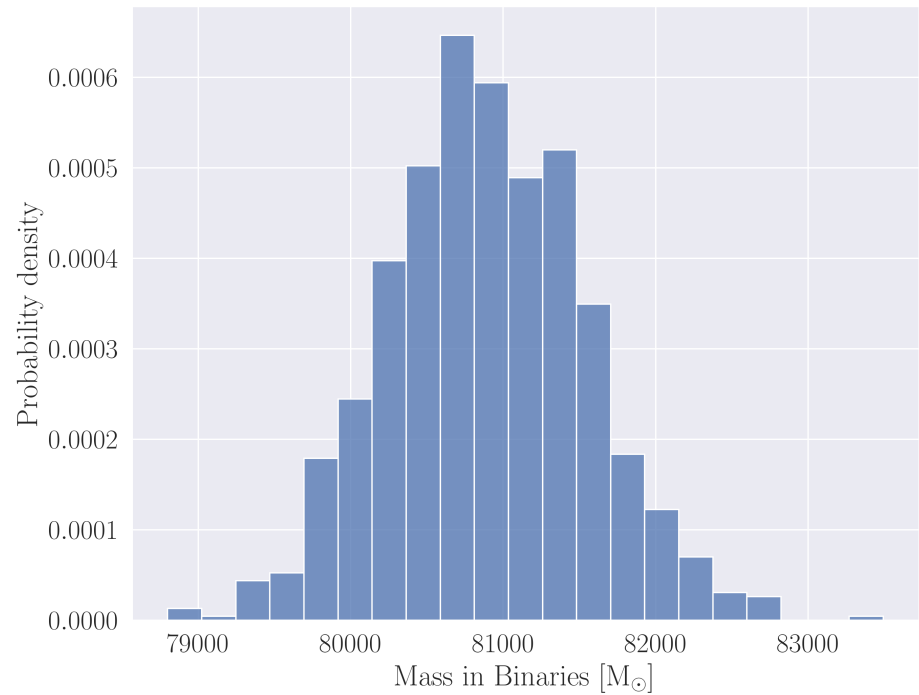


Figure 3.7: Distribution of mass in binaries for models with a 10% binary fraction.

# Chapter 4

## Discussion

In each set of models, all observables are very well reproduced, showing the flexibility of the LIMEPY models. Due to this flexibility, it is unlikely that with current observations we would be able to infer anything about the binary population of a cluster using this technique. Instead, this method should be used in cases where there are existing estimates of the binary population within a cluster in order to add a realistic binary component to LIMEPY models

### 4.1 The Effects of the Binaries

Table 4.1 shows the recovered parameters for each set of models. We can see a clear agreement in the recovered values of the parameters which affect the overall structure of the cluster. In particular, the total cluster mass, half-mass radius, anisotropy radius, truncation parameter, degree of mass segregation and distance are all either identical or within  $1\sigma$  of each other for all three sets of models.

The most striking change in model parameters are the values pertaining to the mass function, in particular, the  $\alpha_3$  parameter which controls the slope of the high-mass mass function (above  $1.0 M_\odot$ ). In the case with a 10% binary fraction, this parameter is much larger than in the other two cases showing that the abundance of binary stars reduces the need for high-mass stars and remnants.

Table 4.1: Best-fit parameters with  $1\sigma$  credibility intervals for all sets of models.

Parameter	Value		
$f_b$	0%	2%	10%
$W_0$	$6.26^{+0.11}_{-0.10}$	$6.28^{+0.10}_{-0.10}$	$6.36^{+0.09}_{-0.09}$
$M/10^6 M_\odot$	$0.88^{+0.01}_{-0.01}$	$0.89^{+0.01}_{-0.01}$	$0.89^{+0.01}_{-0.01}$
$r_h/pc$	$6.73^{+0.06}_{-0.06}$	$6.74^{+0.06}_{-0.06}$	$6.77^{+0.06}_{-0.06}$
$\log_{10} r_a/pc$	$1.50^{+0.07}_{-0.05}$	$1.50^{+0.06}_{-0.05}$	$1.48^{+0.06}_{-0.05}$
$g$	$1.37^{+0.06}_{-0.06}$	$1.36^{+0.06}_{-0.06}$	$1.34^{+0.06}_{-0.06}$
$\delta$	$0.43^{+0.02}_{-0.02}$	$0.43^{+0.02}_{-0.02}$	$0.41^{+0.01}_{-0.01}$
$s^2$	$0.01^{+0.01}_{-0.00}$	$0.01^{+0.01}_{-0.00}$	$0.01^{+0.01}_{-0.00}$
$F$	$3.25^{+0.14}_{-0.12}$	$3.24^{+0.13}_{-0.12}$	$3.16^{+0.13}_{-0.12}$
$\alpha_1$	$0.35^{+0.02}_{-0.02}$	$0.37^{+0.02}_{-0.02}$	$0.45^{+0.02}_{-0.02}$
$\alpha_2$	$1.46^{+0.05}_{-0.05}$	$1.47^{+0.05}_{-0.05}$	$1.53^{+0.05}_{-0.04}$
$\alpha_3$	$2.13^{+0.04}_{-0.04}$	$2.18^{+0.04}_{-0.04}$	$2.46^{+0.05}_{-0.05}$
$BH_{ret}(\%)$	$0.07^{+0.06}_{-0.04}$	$0.08^{+0.09}_{-0.05}$	$0.17^{+0.18}_{-0.12}$
$d$	$4.42^{+0.02}_{-0.02}$	$4.42^{+0.02}_{-0.02}$	$4.43^{+0.02}_{-0.02}$

We can see that there is still some need for black holes in some of the models with a high binary fraction as the  $BH_{ret}$  parameter is much larger in the model with many binaries, this means that even though the initial mass function produces many fewer black holes, more of these black holes need to be retained throughout the evolution of the cluster.

Table 4.2 and Figure 4.2 show the distribution of BHs for each set of models. We can see a clear decrease in the inferred black hole content as we add more binaries though we also note that all three sets of models are consistent with zero black holes within their  $2\sigma$  credibility intervals. This effect of binaries reducing the need for black holes was also found by Mann et al. (2019) (see also associated erratum Mann et al. 2020) when they modelled the central kinematics of 47 Tuc. This effect is due to the high-mass binary systems which have mass-segregated to the central regions of the cluster contributing to the central mass distribution in a similar way to heavy stellar remnants. Through this process, fewer black holes are needed to create the observed

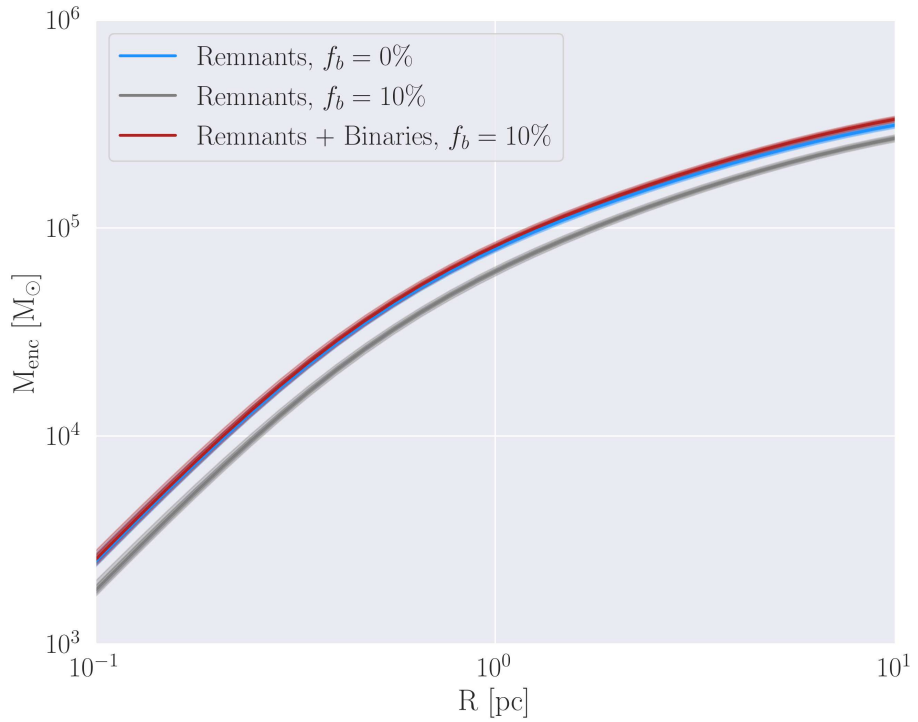


Figure 4.1: Enclosed mass profiles for the stellar remnants in the  $f_b = 0\%$  model and the remnants and remnants plus binaries in the  $f_b = 10\%$  model. The two remnant profiles are very different between the  $f_b = 0\%$  and  $f_b = 10\%$  cases which mirrors the lower black hole content. The most interesting part of these profiles is the fact that when the *binaries* are added to the remnants the enclosed mass profiles match very well. This demonstrates very clearly that the binaries are filling the same role as the heavy remnants in the central regions of the cluster and explains why adding binaries reduces the need for black holes in the models.

central velocity dispersion. This effect is particularly clear in Figure 4.1 where we examine the enclosed mass profiles of remnants and binaries for the no-binary and high-binary cases.

When we examine the density profiles for the models with a binary fraction of 10% (see Figure 4.3), we can see that the binary stars are indeed more centrally concentrated than typical main-sequence stars as predicted and in the central regions, make up almost all the main-sequence contribution, while they contribute more than

Table 4.2: Black hole content in each set of models

Binary Fraction (%)	Mass in BHs	Number of BHs
0	$135^{+104}_{-92} M_{\odot}$	$26^{+15}_{-15}$
2	$114^{+144}_{-79} M_{\odot}$	$22^{+19}_{-13}$
10	$81^{+121}_{-81} M_{\odot}$	$12^{+13}_{-12}$

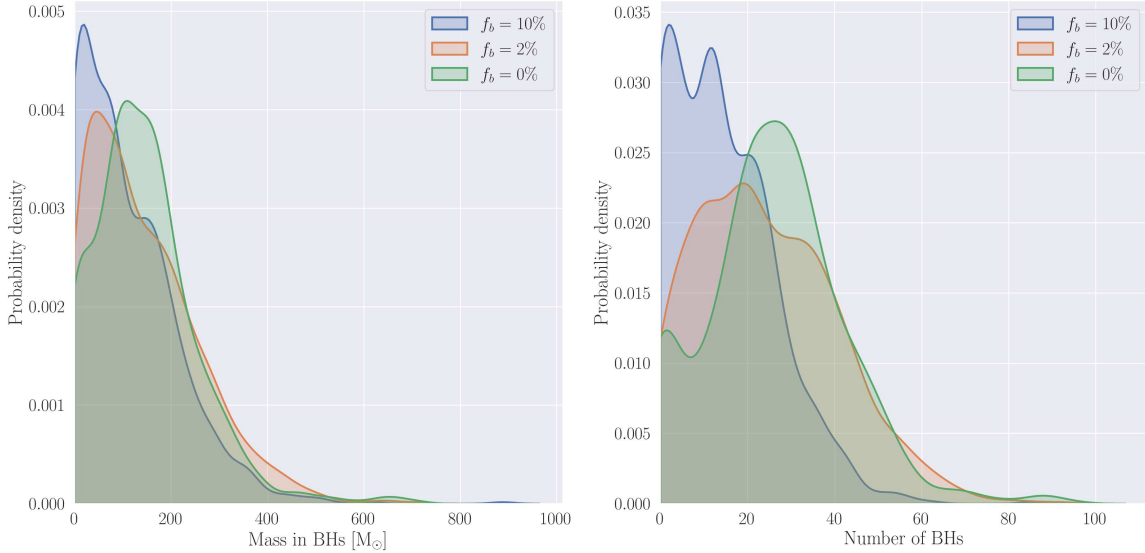


Figure 4.2: Posterior probability distributions of mass and number of BHs in each set of models. Distributions are represented by a Gaussian kernel density estimator of the discrete values for easier visual comparison.

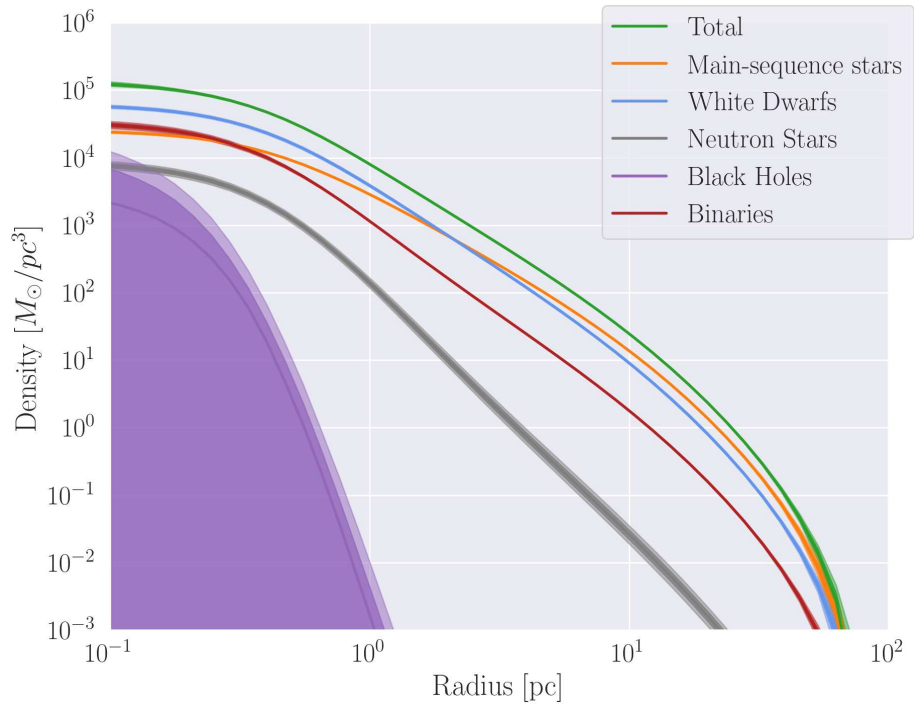


Figure 4.3: Mass density profiles for the models with a binary fraction of 10%

the neutron stars at all radii.

# Chapter 5

## Conclusion

The effects of binary systems have long been a missing ingredient in equilibrium mass models of globular clusters. Due to the effects of mass segregation, heavy binaries will quickly become centrally concentrated, much like heavy remnants. A centrally concentrated population of heavy binary systems could emulate the effects of heavy remnants in the central regions of a cluster and thus by ignoring their effects the remnant populations that we infer for these cluster might be biased.

To investigate this effect we have developed a method to include realistic binary populations in LIMEPY models. We used this method to fit three sets of models to observations of the globular cluster 47 Tuc, a set with no binaries, a set with a binary fraction of 2%, and a set with a binary fraction of 10%. Despite their different binary fractions, all three sets of models were able to satisfactorily reproduce all observables and recovered the same structural parameters for the models. The three sets of models differed primarily in their recovered mass functions and black hole content. As more binaries are added, fewer high-mass remnants are required to reproduce the kinematics of the cluster. This results in a lowered  $\alpha_3$  parameter and less mass in black holes and other heavy remnants.

We further showed how binaries fill the same role as heavy remnants in the central mass distribution of the cluster, explaining why adding binaries to a model reduces

the need for heavy remnants.

The implications of this work depend on the binary fraction of the cluster in question. For 47 Tuc, our best estimates place the binary fraction at around 2%, so this effect is likely negligible. If however, future observations or models suggest that 47 Tuc might be host to more binaries, then it is important that future studies include their effects in their models if they wish to recover accurate remnant populations.

More generally, for clusters where we expect a high binary fraction like, for example, NGC 3201, binaries should certainly be included in any attempts to model the mass distribution of the cluster, especially if the goal is to constrain the population of heavy remnants within the cluster.

## 5.1 Future Work

In this work, we only considered binaries made up of two main sequence stars. In reality, binaries can be formed from any cluster members and binaries where one or both components are heavy remnants would have an even larger effect on the kinematics of the cluster than main-sequence binaries. The reason we did not consider this class of binaries in this project is because we have essentially no constraints on what these populations might look like. The usual photometric methods cannot be used because there is at most one main-sequence star and radial velocity searches will only uncover them if the binary contains a bright star. It's possible that in this case, we could turn to  $N$ -body or Monte Carlo models to constrain the present-day remnant binary populations, but the binary populations in these models are likely to

be highly dependent on the primordial binary population and initial conditions of the models.

In the future it would be a interesting application of this method to examine a cluster like NGC 3201 where we know there is likely to be a fairly large binary population. This might allow us to place stringent and reliable constraints on the black hole population in NGC 3201 while accounting for the degeneracy between black hole content and mass in binaries that we have demonstrated can be important using 47 Tuc as a test case.

# **Appendix A**

# **Supplementary Material**

Table A.1: Pulsar timing data for 47 Tuc, spin periods. Reference key is as follows: a:Freire & Ridolfi (2018), b:Freire et al. (2017), c:Ridolfi et al. (2016)

ID <sup>reference</sup>	$r$ [arcmin]	$P$ [ms]	$\Delta P$ [ms]	$\dot{P}$ [s/s]	$\Delta \dot{P}$ [s/s]	DM [pc/cm <sup>3</sup> ]	$\Delta DM$ [pc/cm <sup>3</sup> ]
aa <sup>a</sup>	0.465	1.8453805296800	$6 \times 10^{-13}$	$-4.5890 \times 10^{-20}$	$0.0015 \times 10^{-20}$	24.971	0.007
ab <sup>b</sup>	0.2092	3.7046394947985	$5 \times 10^{-13}$	$9.820 \times 10^{-21}$	$0.008 \times 10^{-21}$	24.373	0.020
c <sup>b</sup>	1.2298	5.7567799955164	$1 \times 10^{-13}$	$-49.850 \times 10^{-21}$	$0.002 \times 10^{-21}$	24.600	0.004
D <sup>b</sup>	0.6483	5.35757328486572	$7 \times 10^{-14}$	$-3.4219 \times 10^{-21}$	$0.0009 \times 10^{-21}$	24.732	0.003
E <sup>b</sup>	0.6205	3.53632915276243	$3 \times 10^{-14}$	$98.5103 \times 10^{-21}$	$0.0005 \times 10^{-21}$	24.236	0.004
F <sup>b</sup>	0.2149	2.62357935251262	$3 \times 10^{-14}$	$64.5031 \times 10^{-21}$	$0.0007 \times 10^{-21}$	24.382	0.005
G <sup>b</sup>	0.2781	4.0403791435651	$1 \times 10^{-13}$	$-42.159 \times 10^{-21}$	$0.002 \times 10^{-21}$	24.436	0.004
H <sup>b</sup>	0.7677	3.2103407093504	$1 \times 10^{-13}$	$-1.830 \times 10^{-21}$	$0.001 \times 10^{-21}$	24.369	0.008
I <sup>b</sup>	0.2772	3.4849920616629	$1 \times 10^{-13}$	$-45.873 \times 10^{-21}$	$0.002 \times 10^{-21}$	24.429	0.010
J <sup>b</sup>	1.0185	2.10063354535248	$6 \times 10^{-14}$	$-9.7919 \times 10^{-21}$	$0.0009 \times 10^{-21}$	24.588	0.003
L <sup>b</sup>	0.1627	4.3461679994616	$3 \times 10^{-13}$	$-122.0406 \times 10^{-21}$	$0.0010 \times 10^{-21}$	24.400	0.012
M <sup>b</sup>	1.0688	3.6766432176002	$3 \times 10^{-13}$	$-38.418 \times 10^{-21}$	$0.005 \times 10^{-21}$	24.432	0.016
N <sup>b</sup>	0.4793	3.0539543462608	$1 \times 10^{-13}$	$-21.857 \times 10^{-21}$	$0.002 \times 10^{-21}$	24.574	0.009
O <sup>b</sup>	0.0806	2.64334329724356	$4 \times 10^{-14}$	$30.3493 \times 10^{-21}$	$0.0006 \times 10^{-21}$	24.356	0.002
Q <sup>b</sup>	0.9502	4.0331811845726	$2 \times 10^{-13}$	$34.0076 \times 10^{-21}$	$0.0006 \times 10^{-21}$	24.265	0.004
R <sup>b</sup>	0.1519	3.4804627074933	$2 \times 10^{-13}$	$148.351 \times 10^{-21}$	$0.003 \times 10^{-21}$	24.361	0.007
S <sup>b</sup>	0.2150	2.83040595787912	$7 \times 10^{-14}$	$-120.541 \times 10^{-21}$	$0.001 \times 10^{-21}$	24.376	0.004
T <sup>b</sup>	0.3179	7.5884798073671	$9 \times 10^{-13}$	$293.80 \times 10^{-21}$	$0.01 \times 10^{-21}$	24.411	0.021
U <sup>b</sup>	0.9386	4.3428266963923	$1 \times 10^{-13}$	$95.228 \times 10^{-21}$	$0.002 \times 10^{-21}$	24.337	0.004
W <sup>c</sup>	0.087	2.3523445319370	$3 \times 10^{-13}$	$-8.6553 \times 10^{-20}$	$0.0001 \times 10^{-20}$	24.367	0.003
X <sup>c</sup>	3.828	4.77152291069355	$5 \times 10^{-14}$	$1.83609 \times 10^{-20}$	$0.00007 \times 10^{-20}$	24.539	0.005
Y <sup>b</sup>	0.3743	2.19665714352124	$6 \times 10^{-14}$	$-35.1720 \times 10^{-21}$	$0.0008 \times 10^{-21}$	24.468	0.004
Z <sup>b</sup>	0.1506	4.554447383906	$3 \times 10^{-12}$	$-4.56 \times 10^{-21}$	$0.1 \times 10^{-21}$	24.450	0.040

Table A.2: Pulsar timing data for 47 Tuc, orbital periods. Reference key is as follows: a:Freire & Ridolfi (2018), b:Freire et al. (2017), c:Ridolfi et al. (2016)

ID <sup>reference</sup>	$r$ [arcmin]	$P_b$ [day]	$\Delta P_b$ [day]	$\dot{P}_b$ [s/s]	$\Delta \dot{P}_b$ [s/s]	DM [pc/cm <sup>3</sup> ]	$\Delta DM$ [pc/cm <sup>3</sup> ]
E <sup>b</sup>	0.6205	2.2568483	0.0000009	$4.8 \times 10^{-12}$	$0.2 \times 10^{-12}$	24.236	0.004
H <sup>b</sup>	0.7677	2.357696895	0.000000010	$-0.7 \times 10^{-12}$	$0.6 \times 10^{-12}$	24.369	0.008
I <sup>b</sup>	0.2772	0.2297922489	0.0000000004	$-0.8 \times 10^{-12}$	$0.2 \times 10^{-12}$	24.429	0.010
Q <sup>b</sup>	0.9502	1.1890840496	0.0000000004	$-1.0 \times 10^{-12}$	$0.2 \times 10^{-12}$	24.265	0.004
R <sup>b</sup>	0.1519	0.06623147751	0.0000000006	$0.19 \times 10^{-12}$	$0.04 \times 10^{-12}$	24.361	0.007
S <sup>b</sup>	0.2150	1.2017242354	0.0000000006	$-4.9 \times 10^{-12}$	$0.4 \times 10^{-12}$	24.376	0.004
T <sup>b</sup>	0.3179	1.126176771	0.000000001	$2.5 \times 10^{-12}$	$1.1 \times 10^{-12}$	24.411	0.021
U <sup>b</sup>	0.9386	0.42910568324	0.0000000008	$0.66 \times 10^{-12}$	$0.05 \times 10^{-12}$	24.337	0.004
X <sup>c</sup>	3.828	10.921183545	0.000000001	$6 \times 10^{-12}$	$2 \times 10^{-12}$	24.539	0.005
Y <sup>b</sup>	0.3743	0.5219386107	0.0000000001	$-0.82 \times 10^{-12}$	$0.07 \times 10^{-12}$	24.468	0.004

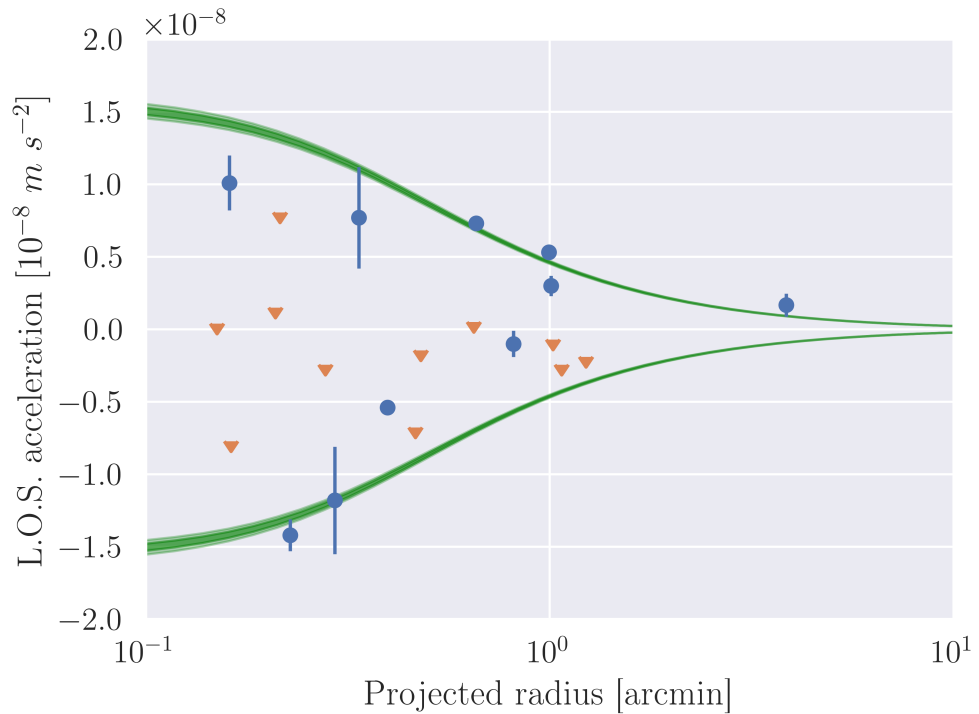


Figure A.1: Maximum acceleration profiles for set of best-fit models with a 0% binary fraction. The accelerations of the pulsars, as derived from their period derivates, are plotted with accelerations derived from orbital periods in blue and upper limits for accelerations derived from spin periods in orange. All accelerations are consistent with the maximum acceleration allowed by the model within their  $1\sigma$  credibility intervals.

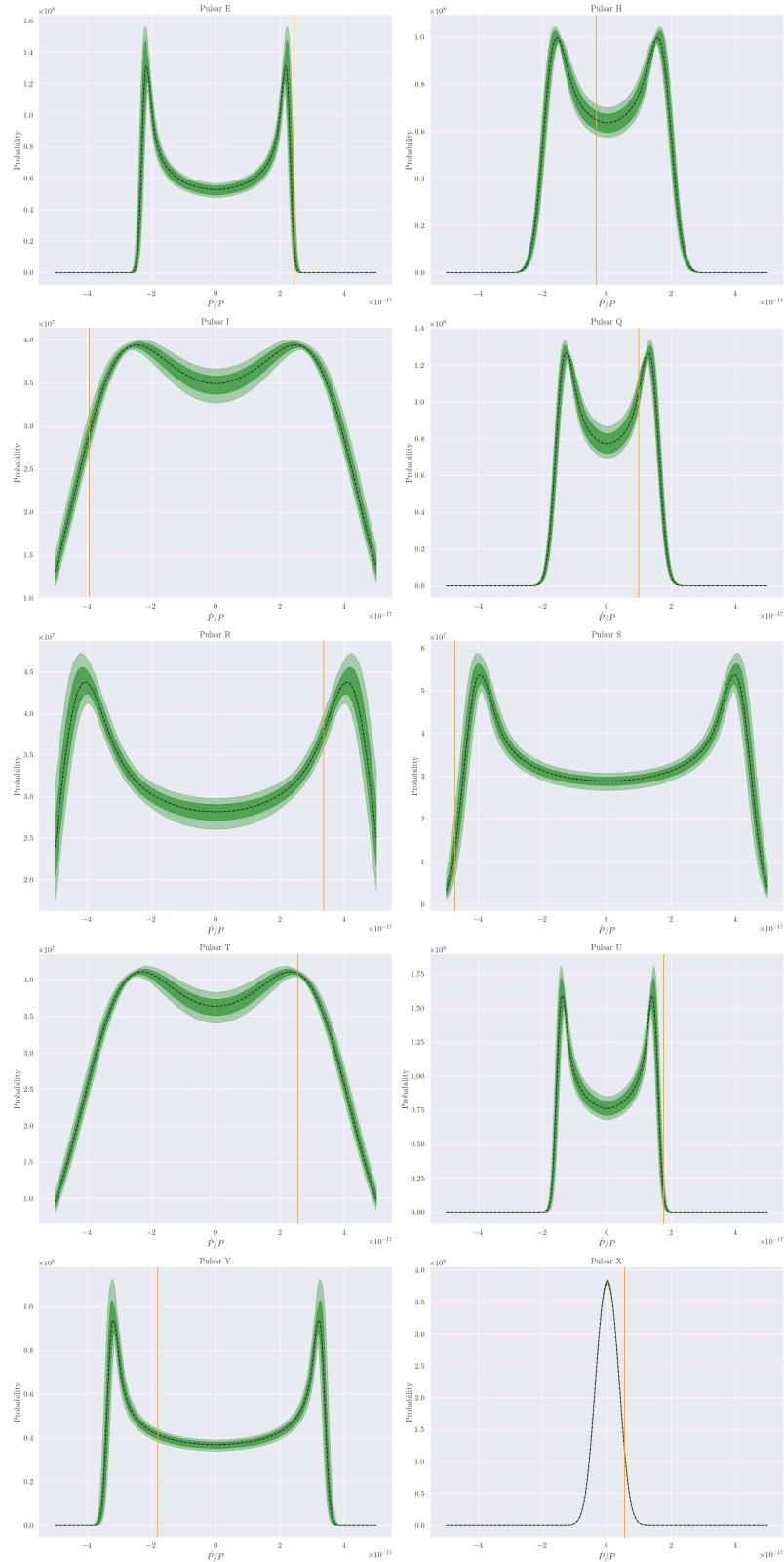


Figure A.2: Probability distributions for measurements of orbital period derivatives for a set of best-fit models with a 0% binary fraction. The measured period derivates for each pulsar are plotted in orange.

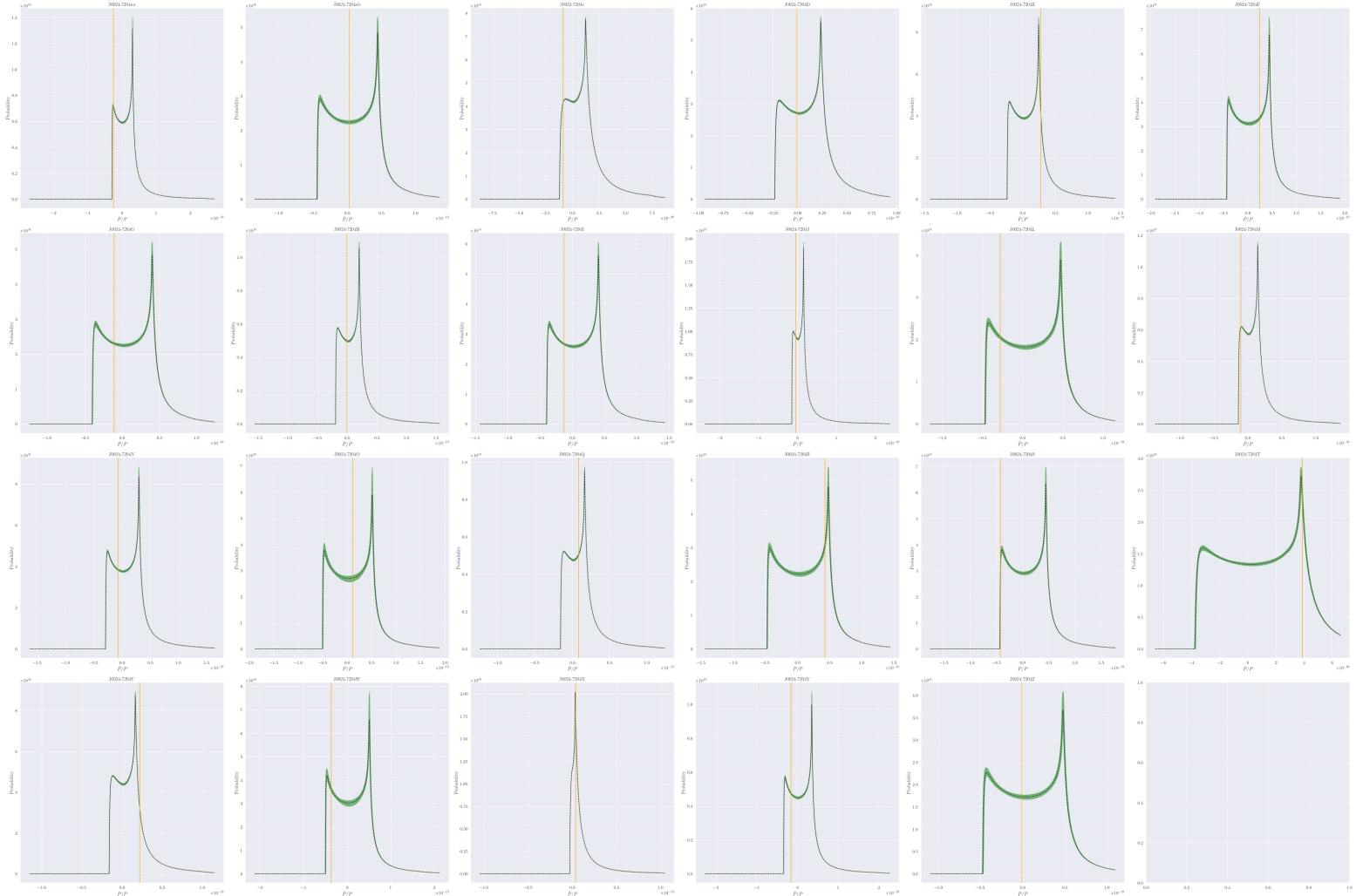


Figure A.3: Probability distributions for measurements of spin period derivatives for a set of best-fit models with a 0% binary fraction. The measured period derivates for each pulsar are plotted in orange.

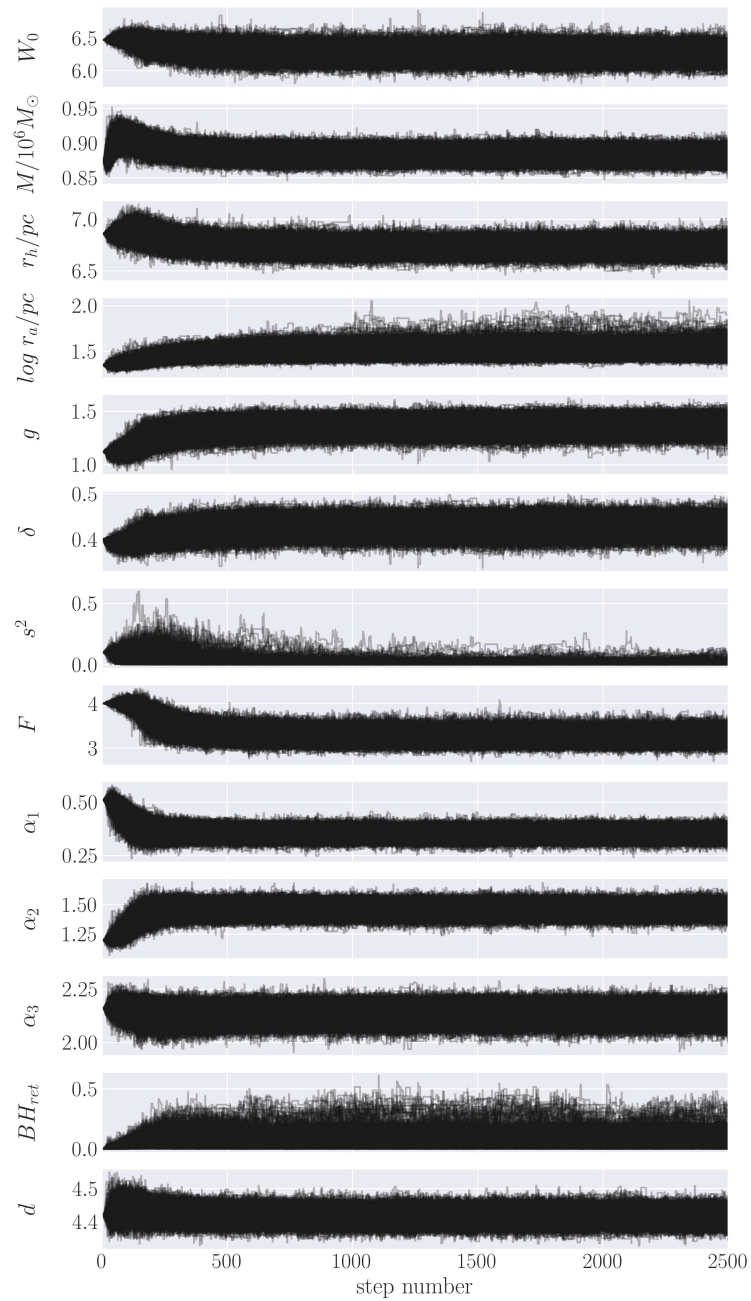


Figure A.4: Trace plot showing the evolution of the MCMC chain for model with a 0% binary fraction.

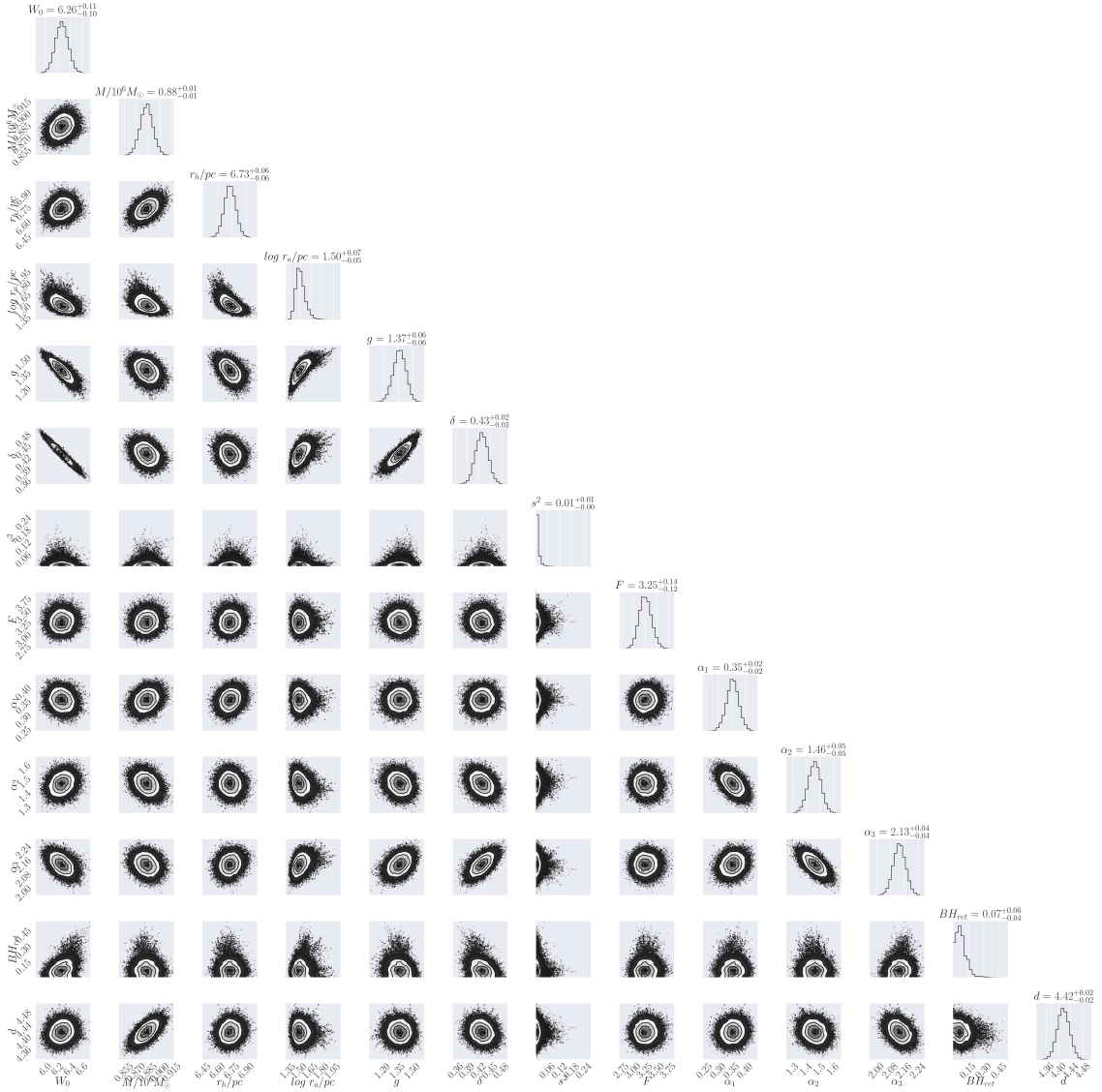


Figure A.5: Corner plot showing the marginalized posterior probability distributions of models parameters with a 0% binary fraction.

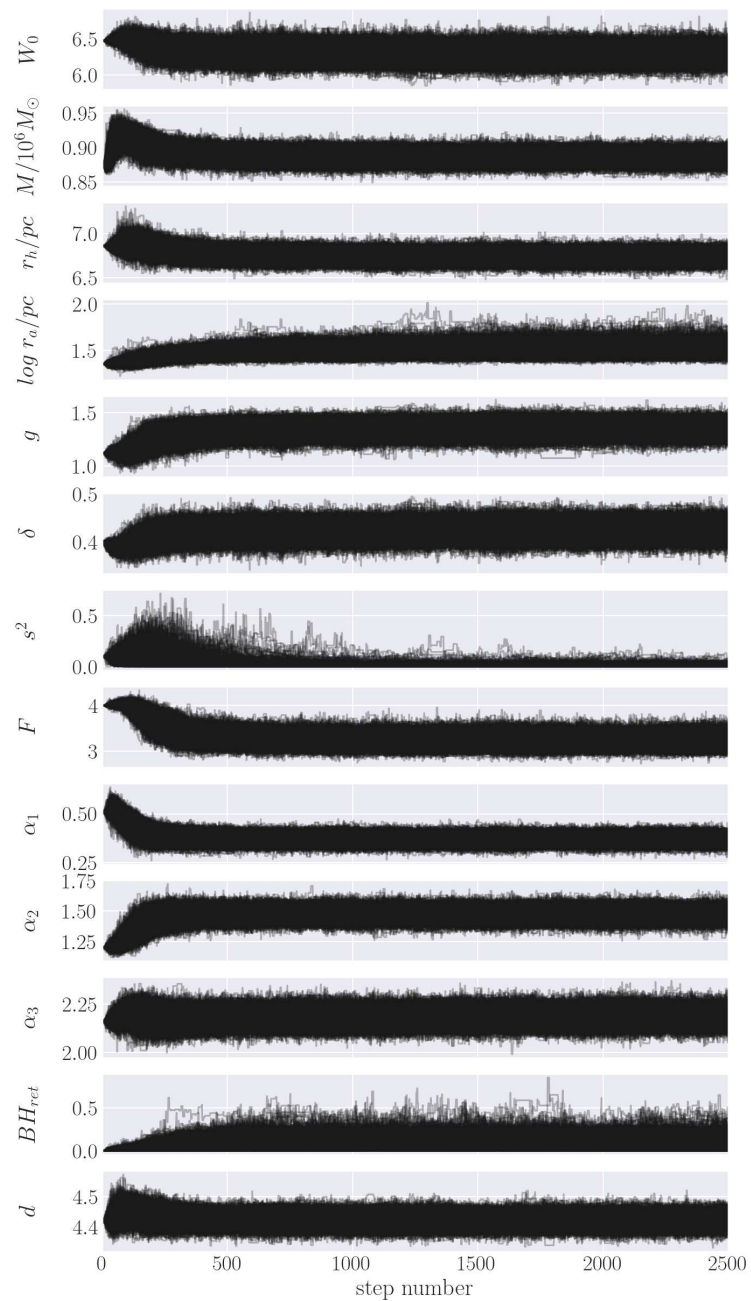


Figure A.6: Trace plot showing the evolution of the MCMC chain for model with a 2% binary fraction.

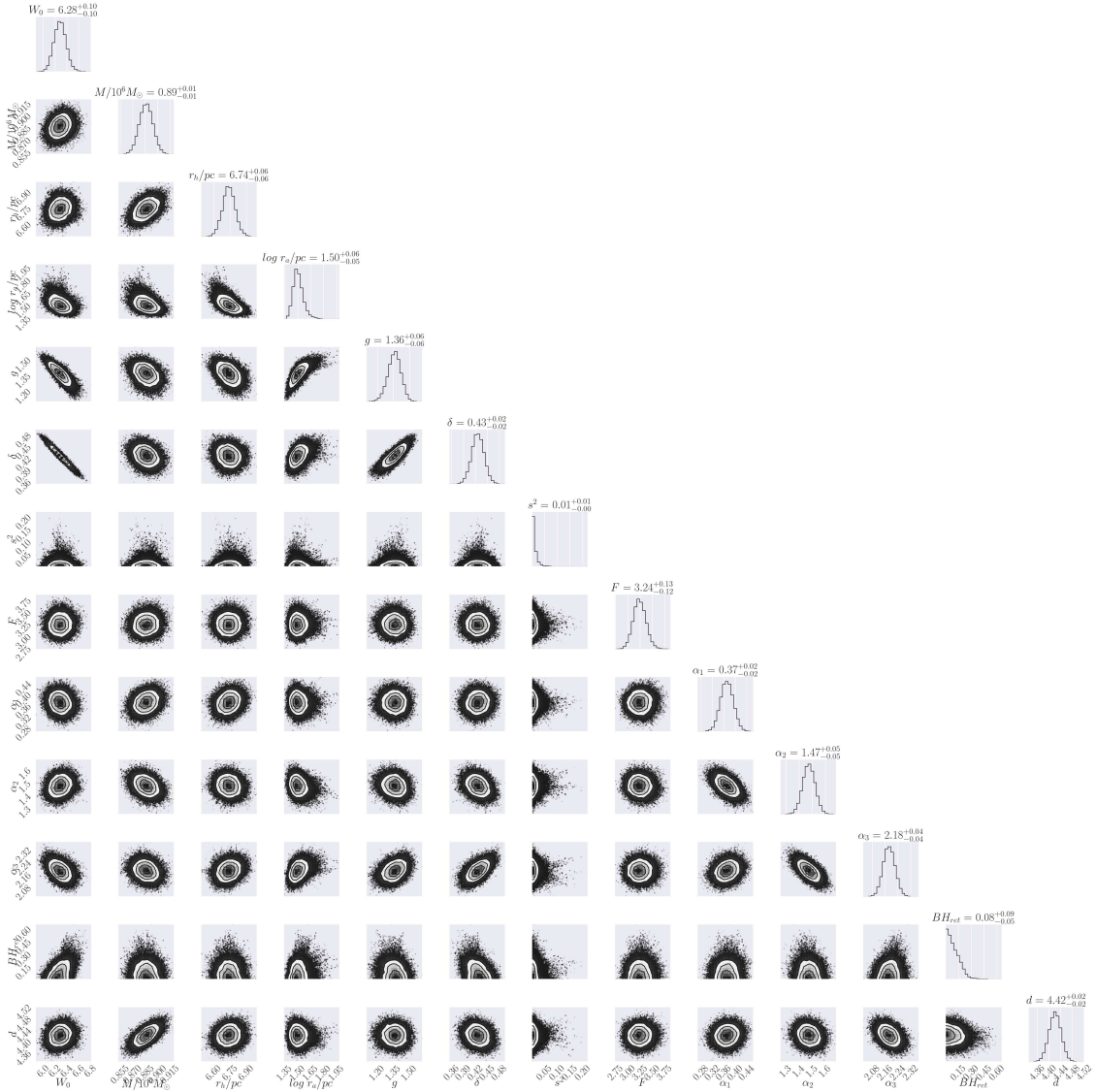


Figure A.7: Corner plot showing the marginalized posterior probability distributions of models parameters with a 2% binary fraction.

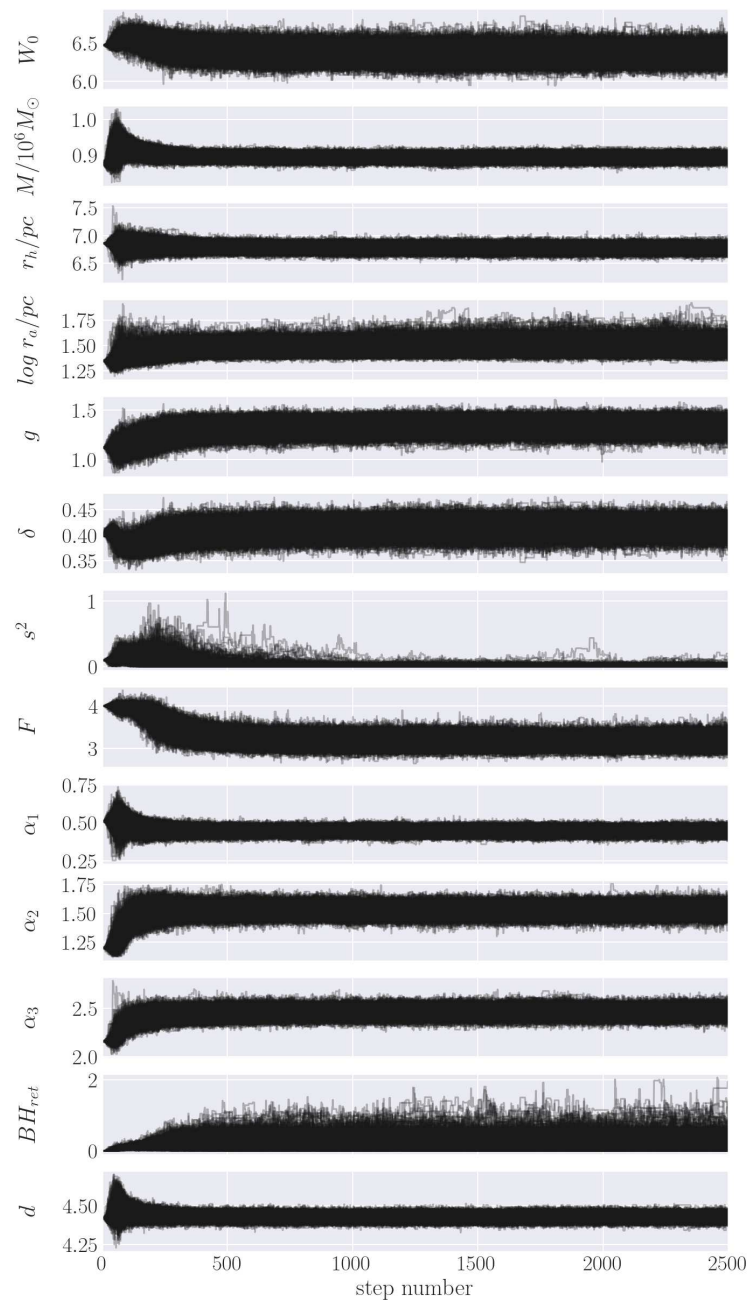


Figure A.8: Trace plot showing the evolution of the MCMC chain for model with a 10% binary fraction.

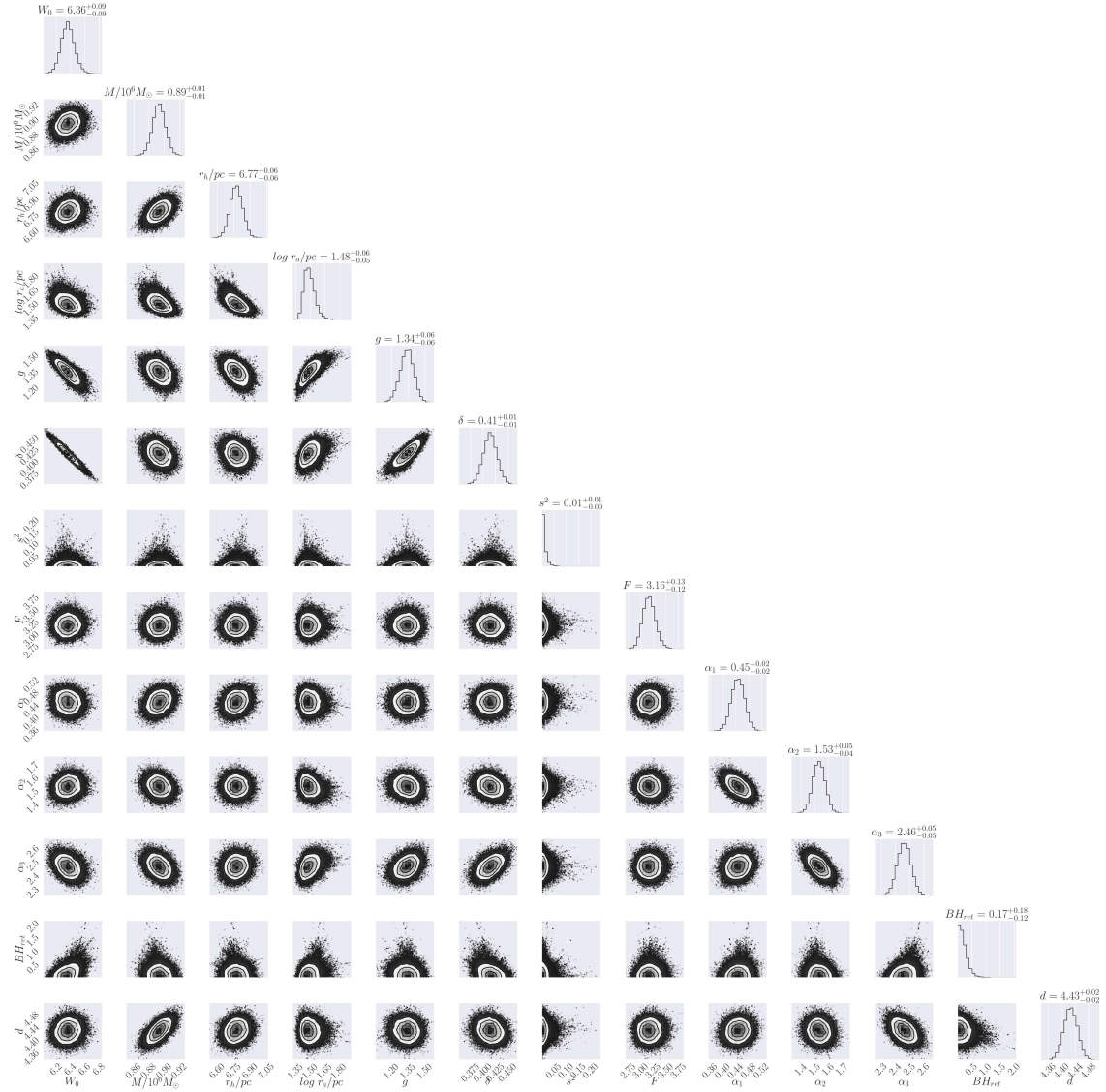


Figure A.9: Corner plot showing the marginalized posterior probability distributions of models parameters with a 10% binary fraction.

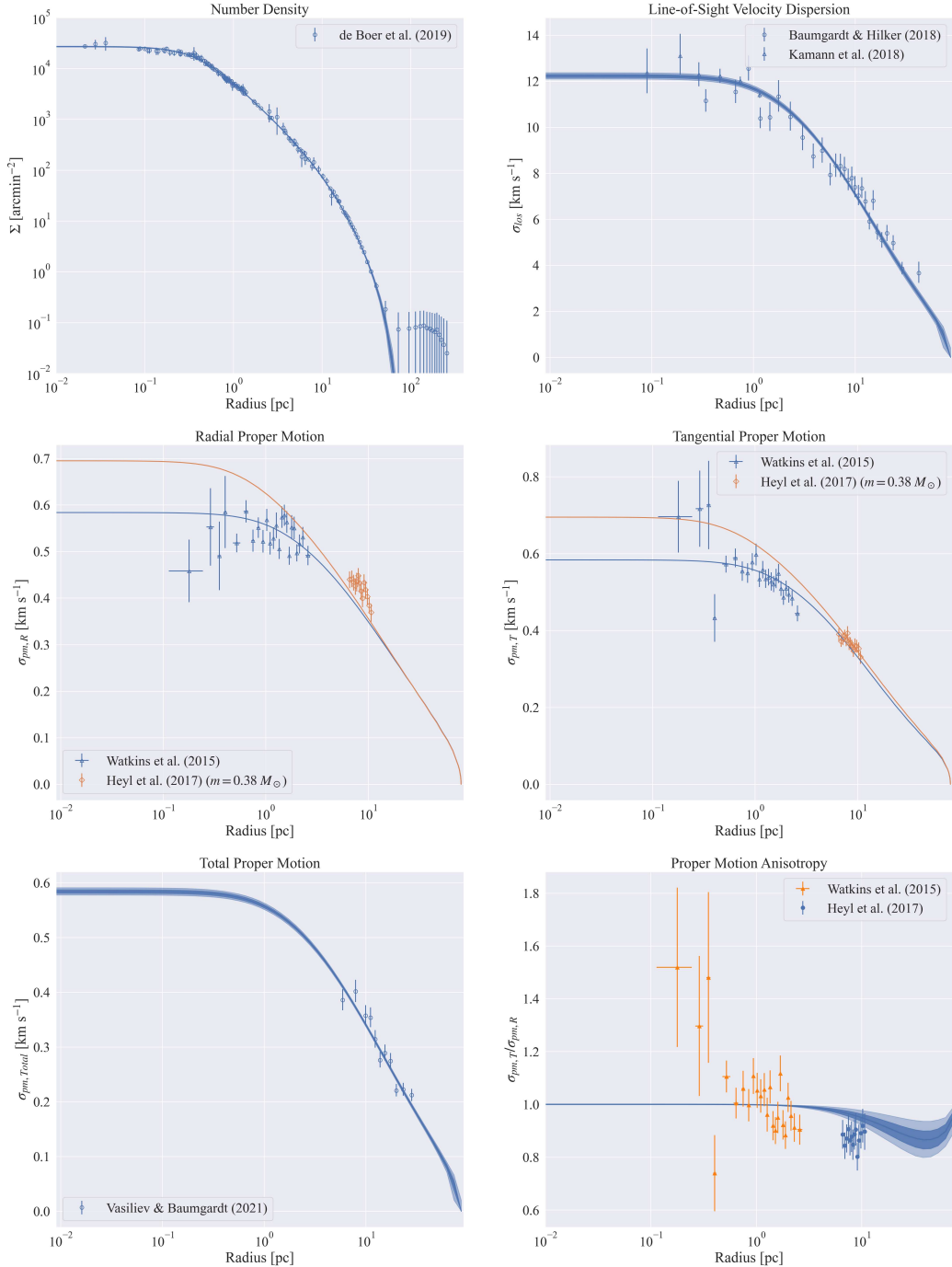


Figure A.10: Model fits to the observables for models with no binary stars.

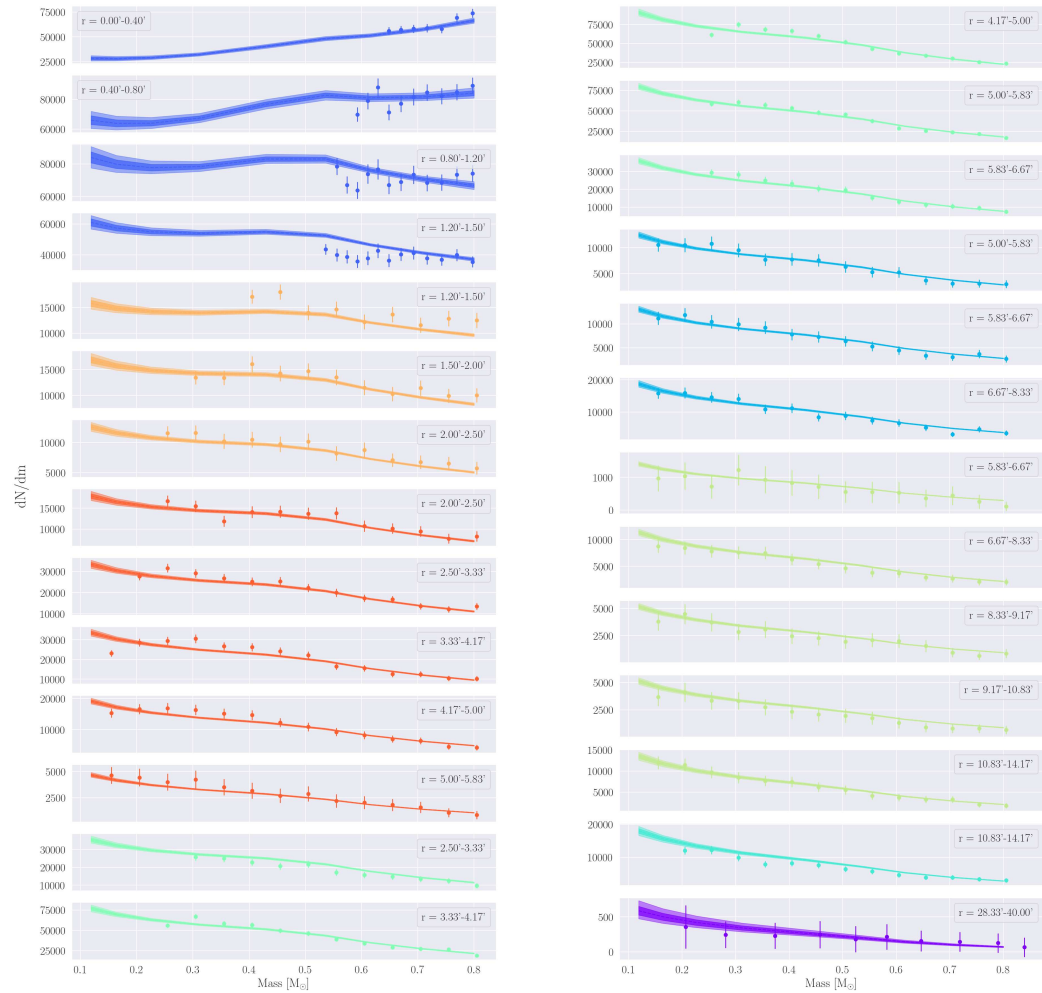


Figure A.11: Model fits to stellar mass function data for models with no binary stars.

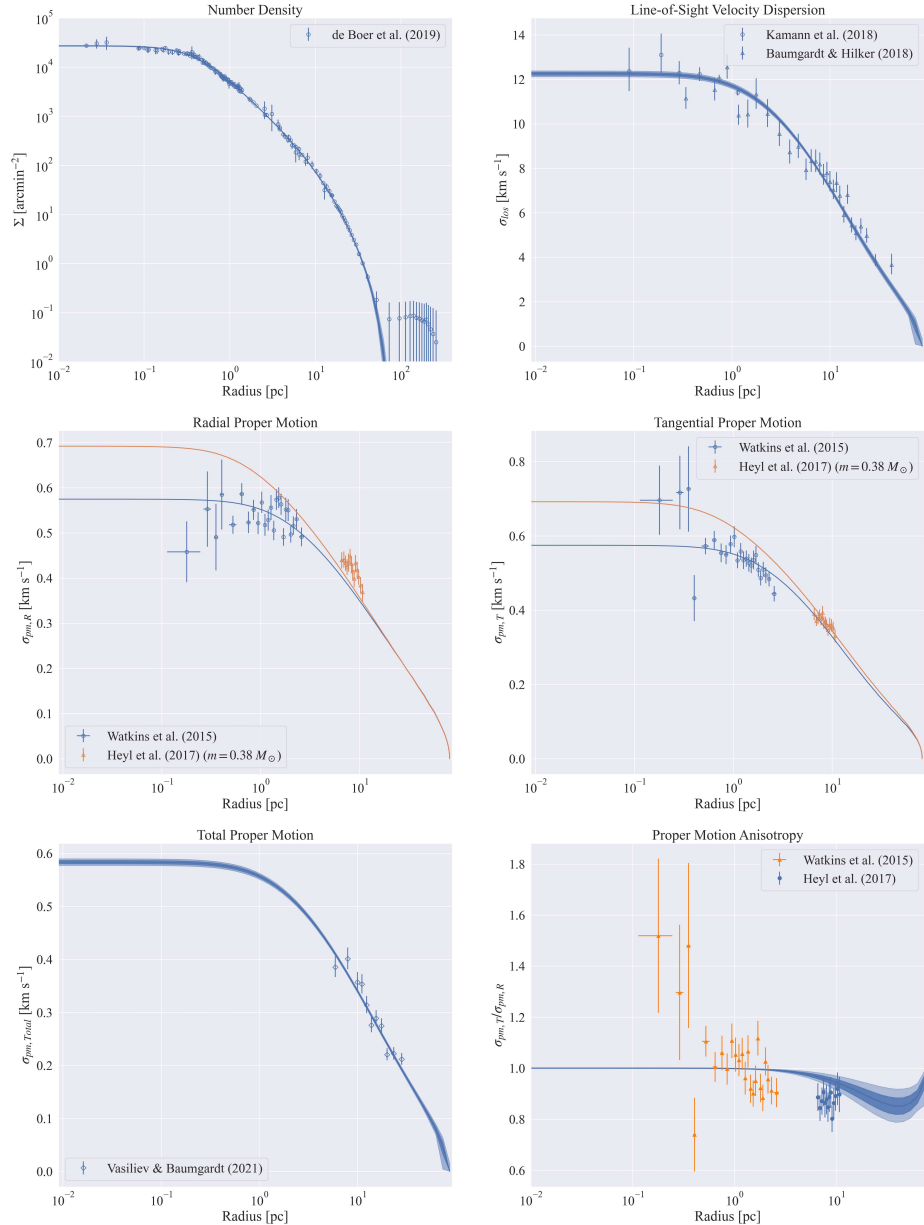


Figure A.12: Model fits to the observables for models with a 10% binary fraction.

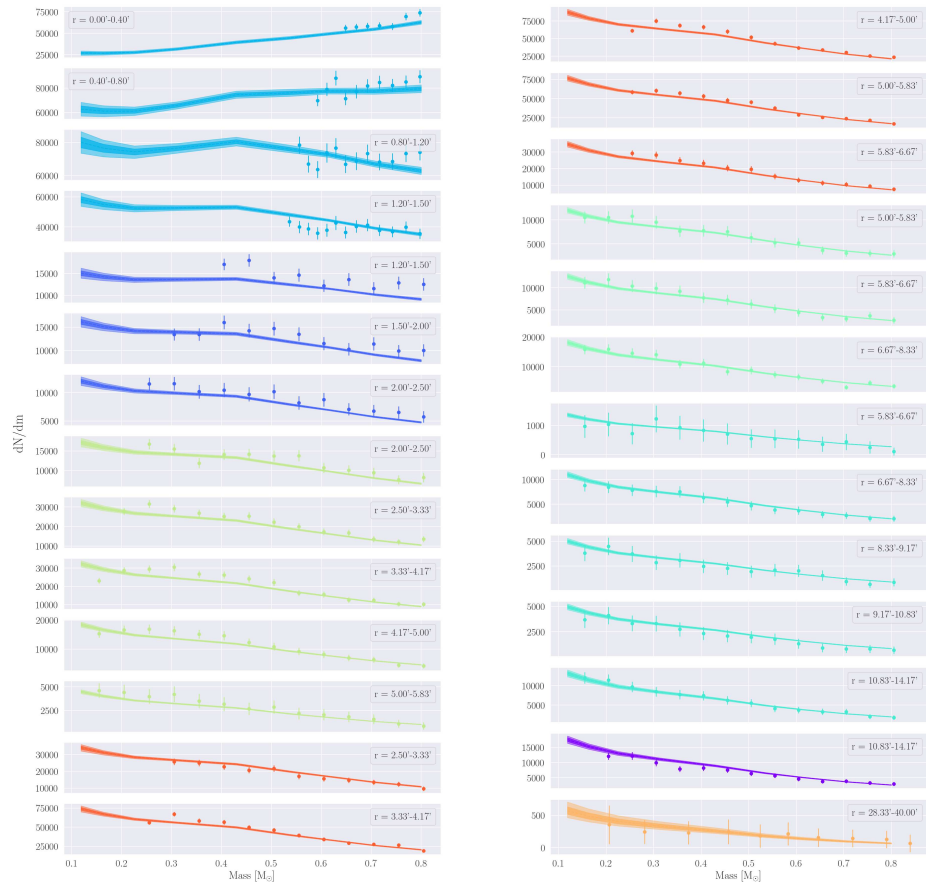


Figure A.13: Model fits to the stellar mass function data for models with a 10% binary fraction.

# Bibliography

- Abbate F., Possenti A., Ridolfi A., Freire P. C., Camilo F., Manchester R. N., D'Amico N., 2018, Monthly Notices of the Royal Astronomical Society, 481, 627
- Balbinot E., Gieles M., 2018, Monthly Notices of the Royal Astronomical Society, 474, 2479
- Baumgardt H., 2017, Monthly Notices of the Royal Astronomical Society, 464, 2174
- Baumgardt H., Hilker M., 2018, Monthly Notices of the Royal Astronomical Society, 478, 1520
- Baumgardt H., Vasiliev E., 2021, Monthly Notices of the Royal Astronomical Society, 505, 5957
- Bellini A., et al., 2014, Astrophysical Journal, 797, 115
- Chatterjee S., Umbreit S., Fregeau J. M., Rasio F. A., 2013, Monthly Notices of the Royal Astronomical Society, 429, 2881
- Choi J., Dotter A., Conroy C., Cantiello M., Paxton B., Johnson B. D., 2016, The Astrophysical Journal, 823, 102
- Claydon I., Gieles M., Varri A. L., Heggie D. C., Zocchi A., 2019, Monthly Notices of the Royal Astronomical Society, 487, 147
- De Boer T. J., Gieles M., Balbinot E., Hénault-Brunet V., Sollima A., Watkins L. L., Claydon I., 2019, Monthly Notices of the Royal Astronomical Society, 485, 4906
- Dotter A., 2016, The Astrophysical Journal Supplement Series, 222, 8
- Fisher J., Schröder K. P., Smith R. C., 2005, Monthly Notices of the Royal Astronomical Society, 361, 495
- Foreman-Mackey D., 2016, The Journal of Open Source Software, 1, 24
- Foreman-Mackey D., Hogg D. W., Lang D., Goodman J., 2013, Publications of the Astronomical Society of the Pacific, 125, 306
- Foreman-Mackey D., et al., 2019, Journal of Open Source Software, 4, 1864
- Freire P. C., Ridolfi A., 2018, Monthly Notices of the Royal Astronomical Society, 476, 4794

- Freire P. C., et al., 2017, Monthly Notices of the Royal Astronomical Society, 471, 857
- Gieles M., Zocchi A., 2015, Monthly Notices of the Royal Astronomical Society, 454, 576
- Gieles M., Balbinot E., Yaaqib R. I., Hénault-Brunet V., Zocchi A., Peuten M., Jonker P. G., 2018, Monthly Notices of the Royal Astronomical Society, 473, 4832
- Giersz M., Leigh N., Hypki A., Lützgendorf N., Askar A., 2015, Monthly Notices of the Royal Astronomical Society, 454, 3150
- Giesers B., et al., 2019, Astronomy & Astrophysics, 632, A3
- Heggie D. C., 1975, Monthly Notices of the Royal Astronomical Society, 173, 729
- Heggie D., Hut P., 2003, The Gravitational MillionBody Problem. Cambridge University Press, doi:10.1017/CBO9781139164535, <https://www.cambridge.org/core/product/identifier/9781139164535/type/book>
- Hénault-Brunet V., Gieles M., Sollima A., Watkins L. L., Zocchi A., Claydon I., Pancino E., Baumgardt H., 2019, Monthly Notices of the Royal Astronomical Society, 483, 1400
- Hénault-Brunet V., Gieles M., Strader J., Peuten M., Balbinot E., Douglas K. E., 2020, Monthly Notices of the Royal Astronomical Society, 491, 113
- Hénon M., 1971, Astrophysics and Space Science, 13, 284
- Heyl J., Caiazzo I., Richer H., Anderson J., Kalirai J., Parada J., 2017, The Astrophysical Journal, 850, 186
- Hypki A., Giersz M., 2013, Monthly Notices of the Royal Astronomical Society, 429, 1221
- King I. R., 1966, The Astronomical Journal, 71, 64
- Kremer K., Ye C. S., Chatterjee S., Rodriguez C. L., Rasio F. A., 2019, Proceedings of the International Astronomical Union, 14, 357
- Mann C. R., et al., 2019, The Astrophysical Journal, 875, 1
- Mann C. R., et al., 2020, The Astrophysical Journal, 893, 86
- Milone A. P., et al., 2012, Astronomy and Astrophysics, 540, A16
- Peuten M., Zocchi A., Gieles M., Hénault-Brunet V., 2017, Monthly Notices of the Royal Astronomical Society, 470, 2736
- Portegies Zwart S. F., Baumgardt H., Hut P., Makino J., McMillan S. L., 2004, Nature, 428, 724

- Reggiani M., Meyer M. R., 2013, *Astronomy & Astrophysics*, 553, A124
- Ridolfi A., et al., 2016, *Monthly Notices of the Royal Astronomical Society*, 462, 2918
- Rodriguez C. L., et al., 2022, *The Astrophysical Journal Supplement Series*, 258, 22
- Sollima A., Baumgardt H., 2017, *Monthly Notices of the Royal Astronomical Society*, 471, 3668
- Trager S. C., King I. R., Djorgovski S., 1995, *The Astronomical Journal*, 109, 218
- VandenBerg D. A., Brogaard K., Leaman R., Casagrande L., 2013, *The Astrophysical Journal*, 775, 134
- Watkins L. L., Van Der Marel R. P., Bellini A., Anderson J., 2015, *Astrophysical Journal*, 812, 149
- Weatherford N. C., Chatterjee S., Kremer K., Rasio F. A., 2020, *The Astrophysical Journal*, 898, 162
- Weatherford N. C., Fragione G., Kremer K., Chatterjee S., Ye C. S., Rodriguez C. L., Rasio F. A., 2021, *The Astrophysical Journal Letters*, 907, L25
- Wilson C. P., 1975, *The Astronomical Journal*, 80, 175
- Woolley R. v. d. R., 1954, *Monthly Notices of the Royal Astronomical Society*, 114, 191
- Zocchi A., Gieles M., Hénault-Brunet V., Varri A. L., 2016, *Monthly Notices of the Royal Astronomical Society*, 462, 696
- Zocchi A., Gieles M., Hénault-Brunet V., 2017, *Monthly Notices of the Royal Astronomical Society*, 468, 4429